

# Mapping molecular models to continuum theories for partially miscible fluids

Colin Denniston<sup>1,2</sup> and Mark O. Robbins<sup>1</sup>

<sup>1</sup>*Department of Physics and Astronomy,*

*The Johns Hopkins University, Baltimore, Maryland 21218, USA and*

<sup>2</sup>*Department of Applied Mathematics,*

*The University of Western Ontario,*

*London, Ontario N6A 5B8, Canada*

(Dated: June 11, 2018)

## Abstract

We map molecular dynamics simulations of fluid-fluid interfaces onto mesoscale continuum theories for partially miscible fluids. Unlike most previous work, we examine not only the interface order parameter and density profiles, but also the stress. This allows a complete mapping from the length scales of molecular dynamics simulations onto a mesoscale model suitable for a lattice Boltzmann or other mesoscale simulation method. Typical assumptions of mesoscale models, such as incompressibility, are found to fail at the interface, and this has a significant impact on the surface tension. Spurious velocities, found in a number of discrete models of curved interfaces, are found to be minimized when the parameters of the mesoscopic model are made consistent with molecular dynamics results. An improved mesoscale model is given and demonstrated to produce results consistent with molecular dynamics simulations for interfaces with widths down to near molecular size.

PACS numbers: 68.05.-n, 47.11.+j, 83.10.Gr, 83.10.Mj

## I. INTRODUCTION

Mesoscale continuum models are increasingly popular for studies of complex fluids [1, 2]. Rather than using a constitutive equation for the local stress based purely on some function of strain, these models incorporate a dependence on the internal microstructure by including the evolution of a local order parameter. They have met with success in describing bulk properties of some materials, such as shear thinning in liquid crystals [3], shear banding flows [4], and phase ordering in binary fluids [5]. However, their treatment of interfacial stresses has not been tested for consistency with large scale molecular simulations. This is an important omission since the detailed interfacial behavior can have a dramatic influence on macroscopic flows.

One example where molecular scale interfacial properties are important is in pinchoff of fluid drops. In cases where a fluid drop breaks up due to some external force, there can be a cascade of instabilities down to microscopic length scales [6]. How such instabilities are cutoff is a question of active research [7] with practical applications to coatings of micro-particles [8]. Another example is dynamic wetting [9]. When a liquid-liquid interface intersects a stationary solid boundary it makes a well defined angle with the solid known as the contact angle. When the solid is moving, the *dynamic* contact angle  $\theta_d$  is a function of the wall velocity. There is significant interest in reproducing this velocity dependence within mesoscopic models [10]. However,  $\theta_d$  is affected by details of the fluid-fluid interface and the solid-fluid interface that are currently unknown. Quantitatively reproducing these effects requires a detailed examination of the microscopic structure of the interfaces near the contact point and how this information can be mapped to the scale of continuum models [11].

The difficulty in selecting an appropriate model is that many different parameters in the mesoscale model influence the value of some macroscopic property like the surface tension. As a complete set of parameters is unavailable, researchers are led to pick parameter sets primarily for convenience, rather than based on some underlying knowledge base. This can lead to significant uncertainties as to the length and time scales for which these models are applicable. Our aim in this paper is to resolve some of this uncertainty in parameter choice, at least for the simple fluid model we examine here. This should then serve as a guide for more complex fluids.

In this paper we examine a binary mixture of simple fluids. The time and distance scales

involved in the hydrodynamic flow and diffusion of such fluids are accessible to molecular dynamics simulations. This allows us to map out the parameters of the mesoscopic model from the molecular simulations. In addition, we can test this mapping by comparing its predictions to simulations for a range of situations not explicitly used in the fits. As methods to map parameters from microscopic to macroscopic models are not well established, we feel it is essential to use simple models that allow extensive testing of the mapping.

The final mesoscale model matches changes in the local stress, as well as order parameter and density profiles, through interfaces in the system. Non-local terms in the free energy, in this case gradients of order parameter and density, are essential for reproducing the observed microscopic stress at interfaces. The results show that many common assumptions are invalid. For example, many models neglect density variations because the bulk fluids are essentially incompressible. Despite this, we find that density variations at the interface still have a significant effect on the interfacial tension. Perhaps more surprising is that some of the elastic constants multiplying gradient terms are negative: The system is stabilized by atomic discreteness at short scales.

In the next section we outline our molecular and mesoscale models, along with the methods we use to simulate them. In Section III we describe the molecular dynamics characterization of both the bulk phases and interfaces of the binary fluid. Fits to various free energy functionals are described in Section IV. A comparison to some simulations of situations not used in the fitting procedure is given in Section V. We conclude with a summary and discussion of implications for further work.

## II. SIMULATIONS AND MODELS

### A. Molecular Scale Model

As we wish to explore a wide range of static and dynamic properties in our model, it is essential that it is kept relatively simple. We will use a model similar to that used by a number of researchers to examine critical properties of fluid mixtures [12], capillary waves [13], and interfacial slip [14, 15, 16]. The model consists of a mixture of two types of molecules, labeled 1 and 2. The interactions between atoms of type  $i$  and  $j$  separated by a

distance  $r$  are modeled using a Lennard-Jones (LJ) potential,

$$V_{ij}(r) = 4\epsilon_{ij} \left[ (\sigma_{ij}/r)^{12} - (\sigma_{ij}/r)^6 \right], \quad (1)$$

where  $\epsilon_{ij}$  specifies the interaction energy and  $\sigma_{ij}$  the interaction length. Unless specified, the force is truncated at the minimum of the potential  $r_c = 2^{1/6}\sigma_{ij}$  to improve computational efficiency. As a result, the interactions are strictly repulsive. For simplicity, all molecules have the same mass  $m$ . For the cases studied here we take  $\sigma_{11} = \sigma_{22} = \sigma_{12} = \sigma$ . Two molecules of the same type interact with the energy scale  $\epsilon_{11} = \epsilon_{22} = \epsilon$ . An extra repulsion is added between unlike molecules  $\epsilon_{12} = \epsilon_{21} = \epsilon(1 + \epsilon^*)$  to control miscibility.

The degree of phase separation is quantified by the order parameter  $\Phi = \rho_1 - \rho_2$ , where  $\rho_1$  and  $\rho_2$  are the local densities of species 1 and 2. Schematics of the phase diagram as a function of density  $\rho$ , temperature  $T$ , and miscibility parameter  $\epsilon^*$  are shown in Fig. 1. For sufficiently high densities the two fluids change from completely miscible to completely immiscible as  $\epsilon^*$  increases (Fig. 1(a)) or  $T$  decreases (Fig. 1(b)). For sufficiently high  $\epsilon^*$  one can observe coexistence of two partially miscible states by adjusting the temperature or density (Fig. 1(c) and (d)).

The object is to map the molecular model to a continuum mean field theory. Thus, we wish to avoid close proximity to a critical point where the behavior is dominated by large scale fluctuations. However, if one is too far from the critical point the interface may be too sharp to be described by mesoscopic models with a continuously varying order parameter. While not obvious a priori, we find that there is a significant range of parameters where mean field theory can be used. The constraints would be even more relaxed in a polymer mixture where, due to the polymer length, the interfaces are broader and the system is more mean-field like. However, the convective-diffusive hydrodynamics of polymer molecules of any significant length are currently inaccessible to molecular dynamics time scales.

Periodic boundary conditions are applied in all three directions of the simulation cell. In systems with interfaces, we take the period in the  $x$ -direction  $L_x$  to be 3–6 times larger than the periods in the other directions, which are usually equal. Most results are reported for systems with 16384 molecules that are roughly evenly divided between type-1 and type-2. The total mean density was varied between  $\rho = 0.83 m/\sigma^3$  and  $\rho = 0.925 m/\sigma^3$ . For the system with  $\rho = 0.85 m/\sigma^3$ , the system size was  $L_y = L_z = 16.1\sigma$  and  $L_x = 74.36\sigma$ . A typical system configuration is shown in Fig. 2.

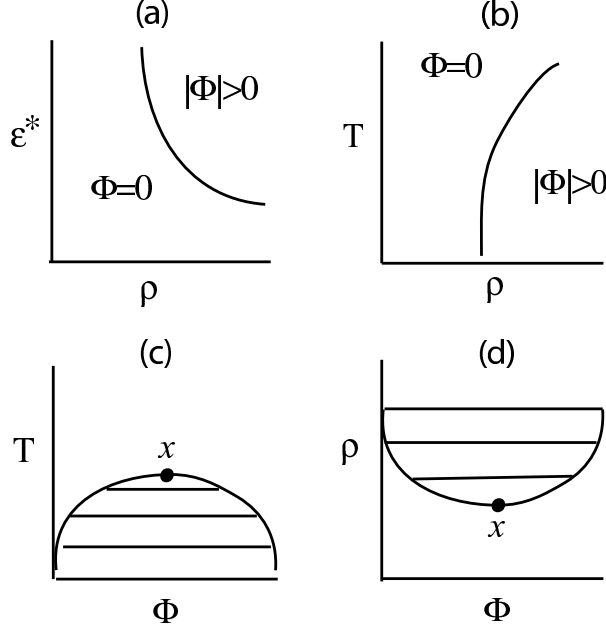


FIG. 1: Schematic slices through the phase diagram at (a) constant temperature, (b) constant  $\epsilon^*$ , (c) constant  $\epsilon^*$  and  $\rho$ , and (d) constant  $T$  and  $\epsilon^*$ . In (c) and (d) the horizontal lines tie coexisting phases and  $x$  marks a critical point.

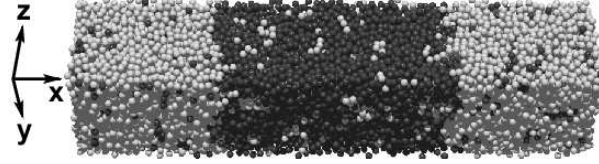


FIG. 2: A liquid-liquid interface between Lennard-Jones fluids at density  $\rho = 0.85m/\sigma^3$ . System size is  $L_x = 74.36\sigma$  and  $L_y = L_z = 16.1\sigma$ , and there are periodic boundary conditions in all three directions. The temperature is  $k_B T/\epsilon = 1.1$  and  $\epsilon^* = 5$ .

To speed up the equilibration time, we supplement the molecular dynamics moves with a Monte Carlo procedure. Every 500 steps, molecules are relabeled (from 1 to 2 or visa versa) according to the Metropolis transition rule. This is a procedure first used for lattice simulations [12] and later extended to molecular dynamics simulations of polymer mixtures [13]. After equilibration, the Monte Carlo routines are turned off.

A characteristic time scale is given by  $\tau = \sigma(m/\epsilon)^{1/2}$ . The molecular dynamics simulations use a time step  $dt = 0.007\tau$ . Typically, we run the simulation for  $5 \times 10^5 dt$  with the Monte Carlo routines turned on. We wait a further  $5 \times 10^5 dt$  to ensure that any convective

flow caused by the relaxation of the initial (nonequilibrium) state has died away. Data is then collected and averaged over the next  $10^7 dt$ .

The motion in the  $y$ -direction, which is always perpendicular to any interfaces in the system, is coupled to a Langevin thermostat [17, 18]. The drag term in the thermostat has a damping rate of  $0.5\tau^{-1}$ . This corresponds to under-damped motion so that even in the  $y$ -direction the motion is dominated by inertia. The equations of motion are integrated using a velocity-Verlet algorithm [18, 19].

The local pressure tensor in a molecular dynamics simulation has the following form [18]

$$\begin{aligned} P_{\alpha\beta}(\mathbf{r}) &= \langle \rho v_\alpha v_\beta \rangle(\mathbf{r}) - \sum_{i,j>i} \left\langle \frac{r_{ij\alpha}}{r_{ij}} \frac{\partial V_{ij}}{\partial r_{ij}} \int_{C_{ij}} dr'_\beta \delta(\mathbf{r} - \mathbf{r}') \right\rangle \\ &= \langle \rho v_\alpha v_\beta \rangle(\mathbf{r}) + \sum_{i,j>i} \langle f_{ij\alpha} \int_{C_{ij}} dr'_\beta \delta(\mathbf{r} - \mathbf{r}') \rangle, \end{aligned} \quad (2)$$

where  $\langle \dots \rangle$  denotes a thermal average,  $C_{ij}$  is a contour joining atoms  $i$  and  $j$  separated by the vector  $\mathbf{r}_{ij}$ , and Greek indices indicate components along the  $x$ ,  $y$ , and  $z$  directions. In what follows, we adopt the summation convention for repeated indices. An apparent ambiguity in Eq.(2) arises from the fact that *any* contour would appear to be acceptable, in that it satisfies microscopic momentum balance. However, requiring the microscopic stress to conform to the symmetry and transformation properties obeyed by the macroscopic stress makes the contour choice unique. The appropriate contour is just the straight line between the two atoms, a choice originally proposed by Irving and Kirkwood [20]. This is true whether or not you impose the additional requirements on the scale of the averages in Eq. (2) [20, 21] or on the corresponding microscopic instantaneous many-body variable inside the averages [22].

Calculating and binning the stress to get local information can be computationally intensive as it needs to be done for every force pair in the system. We developed a new method to minimize this effort. The contour line defined by  $\mathbf{r}_{ij}$  is divided into discrete segments (typically four). The contribution from each segment of the contour is then binned into a spatial grid every four time steps. We choose the number of segments to be high enough to ensure that in steady-state systems the component of the pressure tensor perpendicular to fluid/fluid interfaces is constant, as required by conservation of momentum.

## B. Mesoscale Model

Continuum hydrodynamics is based on conservation laws and the assumption of local equilibrium. The assumption of local equilibrium requires the existence of a free energy density. Further, this free energy density must be expressible as a functional of the density  $\rho$ , temperature  $T$  and order parameter  $\Phi$ . Once determined, this free energy density can be used to calculate the stress tensor and chemical potential required in a full mesoscopic continuum theory.

A number of mesoscale theories are available. Density functional theories based on a weighted density approximation can reproduce the qualitative shape of order parameter and density profiles through static interfaces, although the stress profile does not appear to have been studied [23, 24, 25]. However this approach is computationally challenging because it requires the use of integro-differential equations. Our interest is in models that are easily generalized to nonequilibrium situations so we restrict ourselves to the simplest “non-local” theory, namely one involving local densities and their derivatives. Implementations of such theories come under many names in the literature. Two of the most common are lattice Boltzmann simulations [2, 26] and diffuse interface hydrodynamics [1].

To lowest order in gradients of the total density  $\rho$  and the order parameter  $\Phi$ , the free energy functional can be written as

$$\mathcal{F} = k_B T \int d\mathbf{r} \left\{ \psi + \frac{1}{2} K_\rho (\nabla \rho)^2 + \frac{1}{2} K_\Phi (\nabla \Phi)^2 + K_{\rho\Phi} \nabla \rho \cdot \nabla \Phi \right\}, \quad (3)$$

where  $T$  is the temperature,  $k_B$  is Boltzmann’s constant, and the local bulk free energy  $\psi$  and elastic constants  $K$  may be functions of  $\rho$ ,  $\Phi$  and  $T$ . If the two phases have the same density and elastic constants (“symmetric” case), then the free energy density must be an even function of  $\Phi$ . This requires  $K_{\rho\Phi}$  to be identically zero or an odd function of  $\Phi$ . Mappings of the elastic constants used here to those of a few other common parameterizations of the free energy are given in Appendix A.

Conservation of the number  $\mathcal{M}_i$  of particles of each type imposes the constraints

$$\mathcal{M}_1 + \mathcal{M}_2 = \int d\mathbf{r} \rho, \quad (4)$$

$$\mathcal{M}_1 - \mathcal{M}_2 = \int d\mathbf{r} \Phi \quad (5)$$

Thus at equilibrium we wish to minimize the Lagrangian

$$L = \mathcal{F} + \mu_\rho k_B T \left( \mathcal{M}_1 + \mathcal{M}_2 - \int d\mathbf{r} \rho \right) + \mu_\Phi k_B T \left( \mathcal{M}_1 - \mathcal{M}_2 - \int d\mathbf{r} \Phi \right), \quad (6)$$

where  $\mu_\rho$  and  $\mu_\Phi$  are Lagrange multipliers, and the (constant) factors of  $k_B T$  are included for later convenience. The Euler-Lagrange equations give

$$\mu_\rho = \frac{\partial \psi}{\partial \rho} - K_\rho \nabla^2 \rho - K_{\rho\Phi} \nabla^2 \Phi - \frac{\partial K_{\rho\Phi}}{\partial \Phi} (\nabla \Phi)^2, \quad (7)$$

$$\mu_\Phi = \frac{\partial \psi}{\partial \Phi} - K_\Phi \nabla^2 \Phi - K_{\rho\Phi} \nabla^2 \rho. \quad (8)$$

In deriving Eq.(8) we have ignored terms arising from variations of  $K_\rho$  and  $K_\Phi$  with  $\rho$  and  $\Phi$ . Only the variation of  $K_{\rho\Phi}$  with  $\Phi$  is retained as it must be an odd function of  $\Phi$ . The equations obtained upon relaxing these assumptions and the justification for ignoring the extra terms that result are given in Appendix A.

The Lagrangian density  $\mathcal{L}$ ,

$$\begin{aligned} \frac{\mathcal{L}}{k_B T} = & \psi + \frac{1}{2} K_\rho (\nabla \rho)^2 + \frac{1}{2} K_\Phi (\nabla \Phi)^2 + K_{\rho\Phi} \nabla \Phi \cdot \nabla \rho \\ & - \mu_\rho \rho - \mu_\Phi \Phi, \end{aligned} \quad (9)$$

does not contain any explicit dependence on spatial coordinates. As a result, Noether's Theorem [27] can be used to determine the pressure/stress tensor  $\mathbf{P}$ . It implies that conservation of momentum takes the form

$$\nabla \cdot \mathbf{P} = 0 \quad (10)$$

where

$$P_{\alpha\beta} = -\mathcal{L} \delta_{\alpha\beta} + \partial_\alpha \rho \frac{\partial \mathcal{L}}{\partial \partial_\beta \rho} + \partial_\alpha \Phi \frac{\partial \mathcal{L}}{\partial \partial_\beta \Phi}. \quad (11)$$

As this is related to conservation of momentum, we can associate  $\mathbf{P}$  with a nondissipative stress, or pressure tensor. Substituting  $\mathcal{L}$  and the Euler-Lagrange equation for  $\mu_\rho$  gives

$$\begin{aligned} \frac{P_{\alpha\beta}}{k_B T} = & \frac{p_0}{k_B T} \delta_{\alpha\beta} + K_\rho \left[ (\partial_\alpha \rho)(\partial_\beta \rho) - \frac{1}{2} (\partial_\gamma \rho)^2 \delta_{\alpha\beta} \right] \\ & + K_\Phi \left[ (\partial_\alpha \Phi)(\partial_\beta \Phi) - \frac{1}{2} (\partial_\gamma \Phi)^2 \delta_{\alpha\beta} \right] \\ & + K_{\rho\Phi} [(\partial_\alpha \Phi)(\partial_\beta \rho) + (\partial_\alpha \rho)(\partial_\beta \Phi) \\ & - (\partial_\gamma \Phi)(\partial_\gamma \rho) \delta_{\alpha\beta}], \end{aligned} \quad (12)$$

where the hydrostatic pressure  $p_0$  (trace of  $\frac{1}{3}P_{\alpha\beta}$ ) is

$$p_0 = k_B T (\rho \mu_\rho + \Phi \mu_\Phi - \psi), \quad (13)$$

and the expressions for  $\mu_\Phi$  and  $\mu_\rho$  are given in Eqs. (7) and (8). The relations for the pressure tensor  $P_{\alpha\beta}$  and the chemical potential  $\mu_\Phi$  will allow a direct comparison between the molecular and mesoscopic scale.

### C. Lattice Boltzmann Algorithm

Mesoscale schemes, of which lattice Boltzmann algorithms are an example, have proved very successful in simulations of complex fluids [2]. Lattice Boltzmann algorithms can be viewed as a slightly unusual discretization of the equations of motion or as a lattice version of a simplified Boltzmann equation. In the free energy implementation, equilibrium properties of the fluid are naturally incorporated into the algorithm using ideas from statistical mechanics [26]. We use a nine velocity model on a square lattice. Minor problems related to Galilean invariance [26] are removed via a correction term in the second moment [28].

The lattice Boltzmann scheme simulates the full dynamical equations of convective-diffusive hydrodynamics. These include the continuity equation

$$\partial_t \rho + \partial_\alpha \rho u_\alpha = 0, \quad (14)$$

where  $\mathbf{u}$  is the fluid velocity and Greek indices indicate directions. Conservation of momentum takes the form

$$\begin{aligned} \partial_t \rho u_\alpha + \partial_\beta \rho u_\alpha u_\beta = & -\partial_\beta P_{\alpha\beta} \\ & + \frac{\rho \tau_f}{3} \partial_\beta \left[ \left( 1 - 3 \frac{\partial p_0}{\partial \rho} \right) \delta_{\alpha\beta} \partial_\gamma u_\gamma + \partial_\alpha u_\beta + \partial_\beta u_\alpha \right], \end{aligned} \quad (15)$$

where the parameter  $\tau_f$  sets the viscosity  $\eta$ . Finally, there is the convection-diffusion equation,

$$\partial_t \Phi + \partial_\alpha \Phi u_\alpha = \tau_g \left( \Gamma \nabla^2 \mu_\Phi - \partial_\beta \left( \frac{\Phi}{\rho} \partial_\alpha P_{\alpha\beta} \right) \right). \quad (16)$$

The second term on the right, describing a flow-induced diffusion [29], is a common feature of lattice Boltzmann schemes and is usually negligibly small. We set the algorithmic time constant  $\tau_g$  to unity so that  $\Gamma$  is the diffusion constant. Viscous stresses associated with

velocity gradients are not relevant here as all velocities are zero. However, we will make use of these terms in future works.

To compare the results of the lattice Boltzmann simulations to molecular dynamics, it is useful to compare the units used in the simulations. In molecular dynamics we use Lennard-Jones units, that is  $m$ ,  $\sigma$ , and  $\tau$ . Time is discrete with steps of  $dt = 0.007\tau$ . The size of the time step is limited by the requirement that molecular motion on the steep repulsive part of the intermolecular potential must be resolved. In the lattice Boltzmann simulations a discretization of both space  $\Delta x$  and time  $\Delta t$  is required. We will choose  $\Delta x \approx \sigma$  primarily based on the requirement of resolving the interface width. One could, in principle, use a much coarser lattice in the bulk regions. Stability of our lattice Boltzmann scheme requires the lattice Mach number to be less than one. That is, in units where  $\Delta x \equiv \Delta t \equiv 1$ , the speed of sound

$$v_s \approx \sqrt{\partial p_0 / \partial \rho} < 1. \quad (17)$$

In Lennard-Jones units  $v_s \approx \sqrt{50}\sigma/\tau$  for  $\epsilon^* = 5$  (see below) so we take  $\Delta t = 0.1\tau$  so that  $v_s \approx 0.7\Delta x/\Delta t$ .

As discussed in Section IV, the parameters determined from molecular simulations turn out to be qualitatively different from those commonly used in lattice Boltzmann simulations. As such, we had some problems with numerical stability using standard schemes. Stability was improved by using the predictor-corrector scheme [30], rather than the standard Euler scheme. Stability can be further enhanced by iterating the corrector step a few times. This was found to be helpful in the initial steps, especially if a particularly poor initial state was used. In addition, the method for discretization of derivative operators, particularly Laplacian operators, made a significant difference. Including a mixture of derivatives along coordinate directions and those taken along the diagonal direction improved stability.

To fully specify the model for the lattice Boltzmann algorithm, in addition to Eq.(12) for the pressure tensor, we need explicit expressions for  $\mu_\Phi$  and  $p_0$ . These will be derived and

fit in later sections but for reference we list the complete expressions here:

$$\mu_\Phi = \frac{2A_2}{Z} [e_l(\Phi + \Phi_{co}) + e_r(\Phi - \Phi_{co}) - 2e_re_l\Phi] - K_\Phi \nabla^2 \Phi - K_{\rho\Phi} \nabla^2 \rho, \quad (18)$$

$$p_0 = \rho \frac{\partial A_0}{\partial \rho} - A_0 + \frac{1}{Z} \left( \rho \frac{dA_2}{d\rho} - A_2 \right) \times [e_l(\Phi + \Phi_{co})^2 + e_r(\Phi - \Phi_{co})^2 - 2e_re_l(\Phi^2 + \Phi_{co}^2)] + \frac{2\rho A_2}{Z} \frac{d\Phi_{co}}{d\rho} [e_l(\Phi + \Phi_{co}) - e_r(\Phi - \Phi_{co}) - 2e_re_l\Phi] - \rho \left( K_\rho \nabla^2 \rho + K_{\rho\Phi} \nabla^2 \Phi + \frac{\partial K_{\rho\Phi}}{\partial \Phi} (\nabla \Phi)^2 \right), \quad (19)$$

where

$$\begin{aligned} e_r &= \exp(-A_2(\Phi - \Phi_{co})^2/(2\rho k_B T)), \\ e_l &= \exp(-A_2(\Phi + \Phi_{co})^2/(2\rho k_B T)), \\ Z &= e_r + e_l - e_re_l. \end{aligned} \quad (20)$$

### III. MOLECULAR DYNAMICS MEASUREMENTS

As seen in Fig. 1, there are a number of parameters which affect the phase (mixed or separated) of the system. Much of the interesting behavior in binary fluids occurs when two phases coexist, so we will work with systems near the coexistence line. Coexisting phases have the same  $T$  and  $\epsilon^*$ , but  $\rho$  and  $\Phi$  vary through the interface. Unless otherwise stated, simulations are performed at  $k_B T/\epsilon = 1.1$ . The free energy functional Eq. 3 is then determined from simulations at  $\epsilon^* = 5$  and 6.

The location of the coexistence line  $\Phi_{co}(\rho)$ , a section of which is shown in Fig. 3, can be easily found by varying the average density and letting the system equilibrate (a process we accelerate using the Monte Carlo routines). To obtain further information about the free energy in the vicinity of an equilibrium state, we first study the linear response of the system to small perturbations. As we show in Section III A, this furnishes us with the second derivatives of the bulk free energy  $\psi$  and the elastic constants in the equilibrium state. Section III B considers interfacial behavior. The surface tension is evaluated as a function of  $\rho$  and  $T$ , and the effect of capillary waves on the measured interface shape is examined.

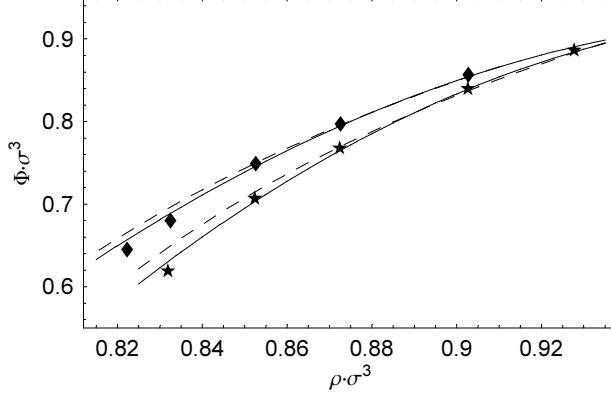


FIG. 3: Portion of the coexistence curve for  $\epsilon^* = 5(\star)$  and  $\epsilon^* = 6(\blacklozenge)$ . The solid line is a quadratic fit to the data and the dashed line is from a fit to Flory-Huggins theory described in Appendix B. Error bars are comparable to the symbol size.

### A. Linear Response of Equilibrium States

We begin with an equilibrated single phase configuration from a molecular dynamics simulation. Thus the 'basis' state has no gradients of any kind. We then add a small force on atoms of type  $i$ ,  $F_i = \delta_i \cos(qx)$ . The forces can be incorporated into the chemical potentials, Eq.(8), as

$$\begin{aligned}\mu_\rho^F &= \mu_\rho - \frac{\delta_1 + \delta_2}{2qk_B T} \sin(qx) + \mathcal{O}(\delta^2), \\ \mu_\Phi^F &= \mu_\Phi - \frac{\delta_1 - \delta_2}{2qk_B T} \sin(qx) + \mathcal{O}(\delta^2),\end{aligned}\quad (21)$$

where  $\mu_\rho$  and  $\mu_\Phi$  are given in Eq.(8). If the  $\delta_i$  are small, we expect a linear response. Then

$$\begin{aligned}\rho &= \rho_0 + \rho_\delta \sin(qx) + \mathcal{O}(\delta^2), \\ \Phi &= \Phi_0 + \Phi_\delta \sin(qx) + \mathcal{O}(\delta^2),\end{aligned}\quad (22)$$

where  $\rho_0$  and  $\Phi_0$  represent the undisturbed state. Plugging this into the previous equations and expanding about the equilibrium state gives

$$\begin{pmatrix} L_{\rho\rho} & L_{\rho\Phi} \\ L_{\Phi\rho} & L_{\Phi\Phi} \end{pmatrix} \begin{pmatrix} \rho_\delta \\ \Phi_\delta \end{pmatrix} \equiv \begin{pmatrix} \frac{\partial^2 \psi}{\partial \rho^2} + K_\rho q^2 & \frac{\partial^2 \psi}{\partial \rho \partial \Phi} + K_{\rho\Phi} q^2 \\ \frac{\partial^2 \psi}{\partial \rho \partial \Phi} + K_{\rho\Phi} q^2 & \frac{\partial^2 \psi}{\partial \Phi^2} + K_\Phi q^2 \end{pmatrix} \begin{pmatrix} \rho_\delta \\ \Phi_\delta \end{pmatrix} = \begin{pmatrix} \frac{\delta_1 + \delta_2}{2qk_B T} \\ \frac{\delta_1 - \delta_2}{2qk_B T} \end{pmatrix} + \mathcal{O}(\delta^2), \quad (23)$$

where the derivatives are about the equilibrium state. By varying the  $\delta_i$  and wave vectors  $q$  we can determine the second derivatives of  $\psi$  and the elastic constants  $K$  of the equilibrium state.

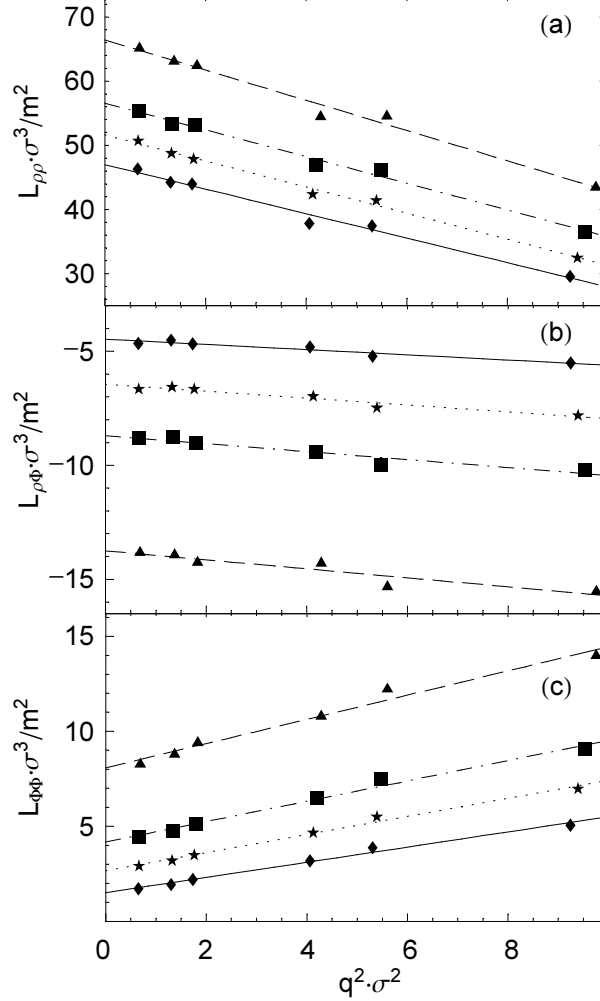


FIG. 4: Linear response coefficients as a function of wave vector squared. The slope of each linear fit (lines) gives an elastic constant and the intercept gives a second derivative of  $\psi$ . The temperature is  $k_B T/\epsilon = 1.1$  and  $\epsilon^* = 6$ . Average density is 0.83 ( $\blacklozenge$ ), 0.85 ( $\star$ ), 0.87 ( $\blacksquare$ ), or 0.9  $m/\sigma^3$  ( $\blacktriangle$ ). Statistical error bars are comparable to symbol sizes.

To separate out the  $q$  dependence we use the following technique. For a given  $q$  we run two simulations, one with  $\delta_1 = \delta_2 = 0.2$  and another with  $\delta_1 = -\delta_2 = 0.1$ . This gives us four equations to determine the four elements of the coefficient matrix (in reality, we have one extra equation due to the symmetry of the matrix). This process must be repeated for a number of different  $q$  in order to separate out the  $q$  dependence of each term. We obtain results for six  $q$ 's simultaneously by apply perturbations at two different (and incommensurate)  $q$ 's in each of the  $x$ ,  $y$ , and  $z$  directions.

The results for  $\mathbf{L}$  can be seen in Fig. 4. The first thing to note is that the matrix

elements are indeed linear functions of  $q^2$ . This indicates that the square gradient theory, assumed in Eq.(8), is capable of describing this system even at wavelengths as short as  $2\sigma$ . A surprising result is that both  $L_{\rho\rho}$  and  $L_{\rho\Phi}$  have a negative slope, implying that  $K_\rho$  and  $K_{\rho\Phi}$  are both *negative*. This means that the square gradient theory becomes unstable to fluctuations at short wavelengths ( $\sim 1\sigma$ ) where one of the eigenvalues of  $\mathbf{L}$  crosses zero. As this distance is comparable to the molecular separation, fluctuations on shorter scales are unphysical. However, this sets a hard lower limit for the mesh spacing introduced in the lattice Boltzmann simulations. Using a mesh spacing shorter than the typical molecular separation to “improve accuracy” is not only pointless, but will be unstable [31].

It is also interesting to note that  $L_{\rho\rho}$  is considerably larger (5 – 10 times) than the other components. This reflects the fact that it is harder to create fluctuations in density than fluctuations in concentrations. Conversely, a small change in density, such as the one seen in Fig. 7 at an interface, may cost a non-negligible amount of free energy and thereby contribute significantly to the surface tension. We will discuss this point further in the next section.

The second derivatives of the free energy and the elastic constants can be obtained from the linear fits in Fig. 4. Fig. 5 shows the second derivatives of  $\psi$  as a function of  $\rho$ , and Fig. 6 shows the elastic constants plotted against  $\rho$  and/or  $\phi \equiv \Phi/\rho$ . Since values of  $\psi$  and the  $K$ ’s were only evaluated near the coexistence line,  $\Phi_{co}(\rho)$ , the dependence on density and concentration is intertwined. The detailed procedure for finding the functional form of  $\psi$  is discussed in Sect. IV. We focus here on parameterizing the elastic constants because they are important in understanding the interfacial tension results in the next section. Note that the variation of the  $K$ ’s with  $\rho$  and  $\Phi$  was ignored in the chemical potentials of Eqs. (7) and (8). Appendix A explains why the variations discussed below can be ignored in these equations.

To separate the  $\Phi$  and  $\rho$  dependence of the elastic constants we must consider points off the coexistence line. In principal this requires simulations on a two-dimensional grid. However, we find that  $K_\rho$  appears to depend only on  $\rho$ , while  $K_{\rho\Phi}$  and  $K_\Phi$  depend only on the scaled variable  $\phi = \Phi/\rho$ . This is illustrated by including a point,  $\rho = 0.83m/\sigma^3$ ,  $\Phi = 0.79m/\sigma^3$ , in Fig. 6 that is away from the coexistence line. This point collapses on the remaining data when  $K_\rho$  is plotted against  $\rho$  and  $K_{\rho\Phi}$  and  $K_\Phi$  are plotted against  $\phi$ . However, it lies far from the other data when the elastic constants are plotted against the other variable, as illustrated in the plot of  $K_\Phi$  vs.  $\rho$ . Perhaps most surprising is that the

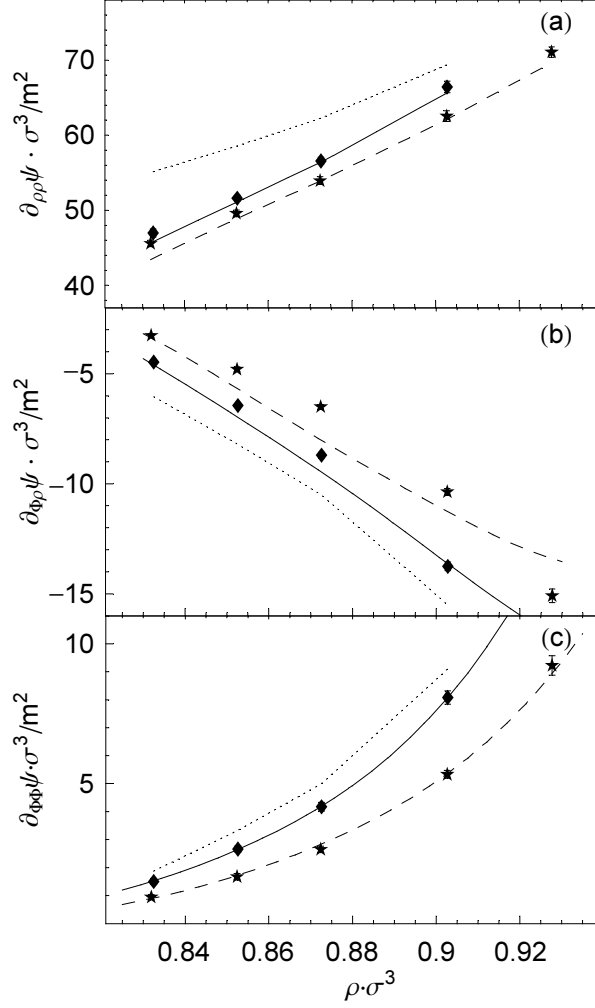


FIG. 5: The second derivatives of  $\psi$  as a function of density along the coexistence line for ( $\diamond$ )  $\epsilon^* = 6$  and ( $\star$ )  $\epsilon^* = 5$ . Data points were obtained from the intercepts of the linear fits in Fig. 4. The second derivatives of the parameterization of  $\psi$  for  $\epsilon^* = 6$  (solid line) and  $\epsilon^* = 5$  (dashed line) given in Section IV and the Flory-Huggins free energy (dotted line) discussed in Appendix B for  $\epsilon^* = 6$  are also shown.

results for different  $\epsilon^*$  also collapse in Fig. 6 (a), (b) and (d). Thus we can fit the data for the elastic constants with one set of parameters.

Given the above results we take  $K_\rho$  independent of  $\Phi$  and fit it to a linear function of  $\rho$  with the result given in Table I. By symmetry,  $K_{\rho\Phi}$  must be an odd function of  $\Phi$ . The dashed line in Fig. 6(b) corresponds to a fit of the data assuming  $K_{\rho\Phi} \sim \phi$  whereas the solid line is a fit assuming  $K_{\rho\Phi} \sim \phi^3$ . The cubic function yields a better fit, giving the result listed in Table I. This suggests that the common practice of neglecting terms involving  $K_{\rho\Phi}$

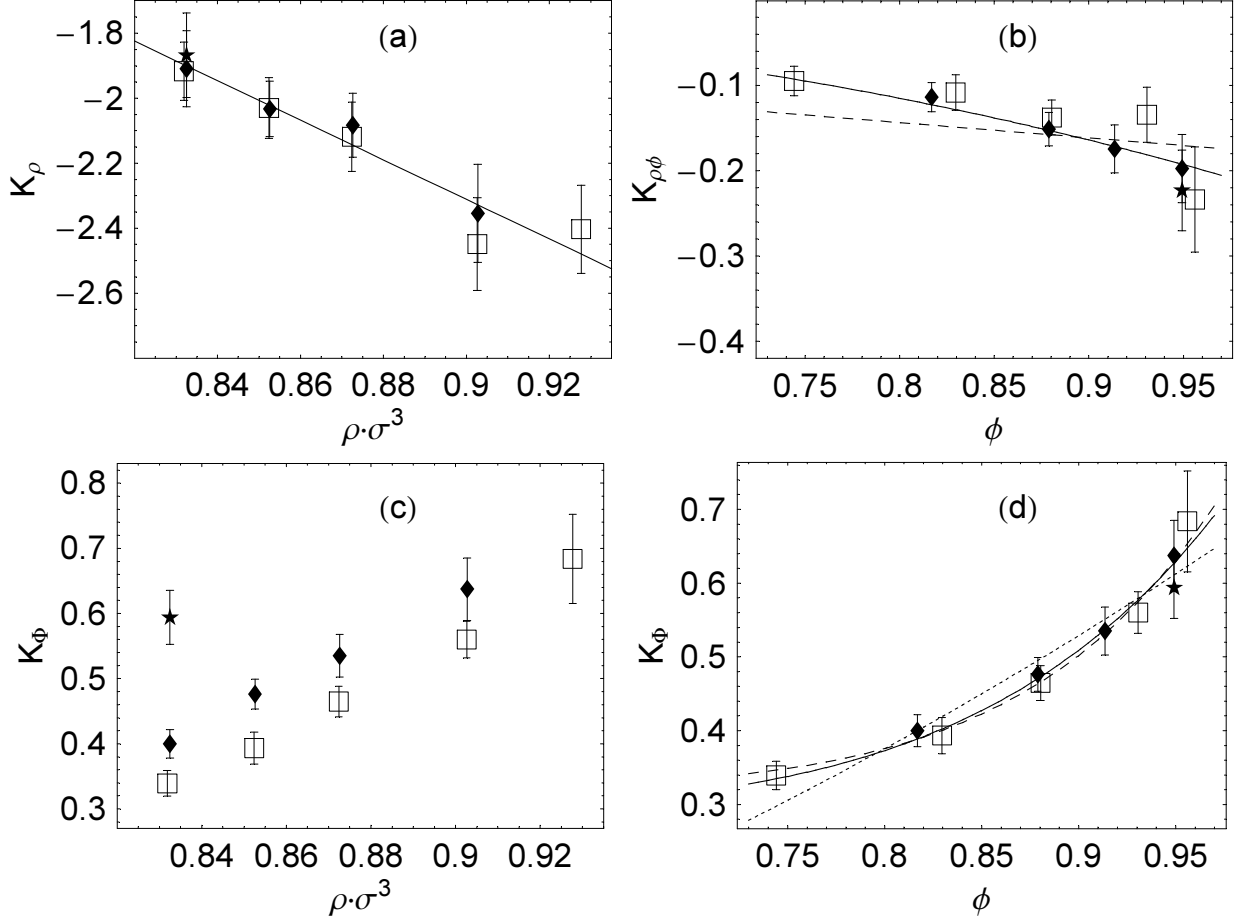


FIG. 6: The elastic constants  $K_\rho$ ,  $K_\Phi$ , and  $K_{\rho\phi}$  as a function of the density  $\rho$  or order parameter  $\phi = \Phi/\rho$ . The points with the  $\square$  symbol are for  $\epsilon^* = 5$  and the  $\blacklozenge$  and  $\star$  symbols are for  $\epsilon^* = 6$ . All systems lie on the coexistence line except the  $\star$  point is off coexistence at  $\rho = 0.83$ ,  $\Phi = 0.79 m/\sigma^3$ . All elastic constants are in units of  $\sigma^5/m^2$ . The lines represent fits given in Table I and described in the text.

is justified in situations where  $\phi$  is small, such as near the critical point, but is not justified in the more typical case considered here.

Symmetry constrains  $K_\Phi$  to be an even function of  $\phi$ . The dotted line in Fig. 6(d) comes from a fit of  $K_\Phi$  to a quadratic function of  $\phi$ . This clearly deviates systematically from the data which appears to be approaching a much flatter function of  $\phi$  as  $\phi \rightarrow 0$ . The solid and dashed lines, which both furnish good fits over the range of data, correspond respectively to the  $\phi^8$  and  $\phi^{10}$  fits given in Table I. As we shall see in the next section, the value of  $K_\Phi$  has a significant impact on interface properties. However, these properties are most

$K_\rho$	$(3.16 \pm 0.5 \frac{\sigma^5}{m^2}) + (-6.08 \pm 0.57 \frac{\sigma^8}{m^3}) \rho$
$K_{\rho\Phi}$	$(-0.225 \pm 0.011 \frac{\sigma^5}{m^2}) \phi^3$
$K_\Phi$	$(0.286 \pm 0.015 \frac{\sigma^5}{m^2}) + (0.517 \pm 0.031 \frac{\sigma^5}{m^2}) \phi^8$ $(0.319 \pm 0.013 \frac{\sigma^5}{m^2}) + (0.524 \pm 0.03 \frac{\sigma^5}{m^2}) \phi^{10}$

TABLE I: Elastic constants measured for  $\epsilon^* = 5$  and 6 and  $0.82m/\sigma^3 < \rho < 0.925m/\sigma^3$ . Care should be taken in extrapolating the elastic constants outside of the measured range. The two alternatives given for  $K_\Phi$  fit equally well over the range of the linear response data ( $0.74 < \phi < 0.97$ ).

strongly dependent on the value of  $K_\Phi$  around  $\phi = 0$ . As such, the fact that  $K_\Phi$  is nearly constant in this region is a highly desirable result. However, in order to have confidence in an extrapolation of  $K_\Phi$  from values of  $\phi > 0.74$  down to  $\phi = 0$  requires that we examine the interfaces explicitly.

## B. Interface characterization

We will examine the geometry shown in Figure 2. There are periodic boundary conditions in all directions and two flat (on average) interfaces normal to the  $x$ -axis. We have examined different runs with average densities ranging from  $\rho = 0.82m/\sigma^3$  to  $\rho = 0.925m/\sigma^3$ , temperatures from  $k_B T/\epsilon = 0.8$  to  $k_B T/\epsilon = 2.0$ , and  $\epsilon^*$  from 5 to 8. Fig. 7 shows  $\Phi$  and  $\rho$  for a typical system at  $k_B T/\epsilon = 0.8$ .

Most models of binary fluids in the literature assume incompressibility and therefore that  $\rho$  is constant. This is a reasonable assumption in the bulk but is violated at an interface, as illustrated in Fig. 7. The density dip in panel (b) is a ubiquitous feature of fluid-fluid interfaces noted recently in several publications [32, 33], including some involving polymer fluids [14, 34]. The dip occurs because the energetically unfavorable 1-2 particle interactions are concentrated at the interface. The system can lower its free energy by decreasing the overall density at the interface as this reduces the number of 1-2 particle interactions. The size of the dip is determined by balancing this energy gain against the entropic cost from denying particles at the interface some volume.

The surface tension associated with the interface is the most important characteristic for

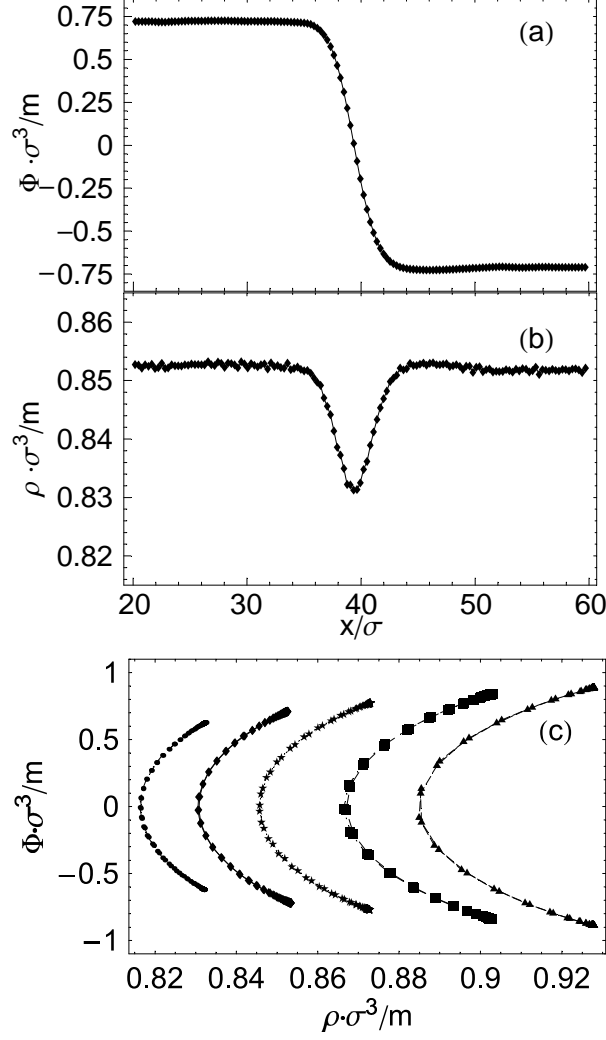


FIG. 7: (a) Order parameter  $\Phi$  and (b) density  $\rho$  along the  $x$ -direction of the simulation box, and averaged over the  $y$  and  $z$  directions. The temperature is  $T = 0.8$  and  $\epsilon^* = 5$ . (c)  $\Phi$  versus  $\rho$  for different interfaces with  $T = 1.1$  and average density of 0.83 ( $\bullet$ ), 0.85 ( $\blacklozenge$ ), 0.87 ( $\star$ ), 0.9 ( $\blacksquare$ ), and 0.925 ( $\blacktriangle$ ).

determining macroscopic behavior. The mechanical definition due to Kirkwood and Buff [35] relates the surface tension to the integral of the difference between the normal  $P_{\perp}$  and parallel  $P_{\parallel}$  components of the pressure tensor across the interface. For a flat interface normal to the  $x$ -axis, this can be written as

$$\gamma = \int [P_{xx}(x) - (P_{yy}(x) + P_{zz}(x))/2] dx. \quad (24)$$

In the quiescent state,  $P_{xx}$  is constant throughout the system (no flow implies  $\partial_{\alpha} P_{\alpha\beta} = 0$  and all quantities are constant in both the  $y$  and  $z$  directions).

Far from the interface the pressure is isotropic and one expects  $P_{xx} = P_{yy} = P_{zz}$ . However, for small systems this expectation fails. For example for  $L_y = L_z = 8.2\sigma$  and  $L_x = 37.8\sigma$  we found that  $P_{\perp} - P_{\parallel} = 0.004$  in a homogeneous system (i.e. without interfaces). Although this sounds small, when it is integrated over the whole system it yields  $(P_{\perp} - P_{\parallel})L_{\perp} = 0.15$ . This integrated stress difference is not related to the surface tension but still gives a significant contribution to Eq.(24). The effect appears to be due to the fact that the density-density correlation function has not decayed to zero at a separation of  $L_y = L_z$  but has by  $L_x$  [16]. This appears to be a significant unrecognized error in molecular dynamics calculations of surface tensions. For the larger systems for which we present data, we find that  $(P_{\perp} - P_{\parallel}) \leq 0.0002$  and  $(P_{\perp} - P_{\parallel})L_{\perp} \leq 0.015$ .

Fig. 8 shows measured surface tensions as a function of density,  $\epsilon^*$ , and temperature. Normally, one expects the surface tension to decrease as you move towards the critical point. This is certainly the case as one decreases the density (Fig. 8(a)). However, the surface tension increases as a function of temperature despite the fact that increasing the temperature moves the system towards the critical point. This effect has been noted before by a number of workers [24, 33]. The surface tension peaks around  $k_B T/\epsilon = 2$  and then starts decreasing [33]. As one increases  $T$ , there is a stronger mixing at the interface that introduces more of the weaker 1 – 2 interactions and raises the potential energy. This leads to an increase in  $\gamma$  until at higher temperatures the entropy contribution brings it back down again [33].

In addition to the surface tension, it is possible to define a characteristic width to the interface. The interface profile for  $\Phi$  from the molecular dynamics simulations (Fig. 7(a)) can be fit to a tanh shape or equally well to an error function  $\text{erf}((x - x_0)/\sqrt{2\xi^2})$ . Similarly  $\rho$  can be fit to a constant minus a Gaussian,  $A \exp(-(x - x_0)^2/(2\xi^2))$ . The resulting widths  $\xi$  are shown in Fig. 9.

The stress profile through the interface also provides useful information. The surface tension is related to the stress through the kernel of Eq.(24),

$$\Gamma(x) \equiv P_{xx}(x) - (P_{yy}(x) + P_{zz}(x))/2, \quad (25)$$

We measure the local components of the stress tensor directly in the molecular dynamics simulations. A typical example is shown in Fig. 10(a). The variation of  $\Gamma$  is also fit to a Gaussian to obtain a width. As shown in Fig. 9, this width is smaller than those obtained

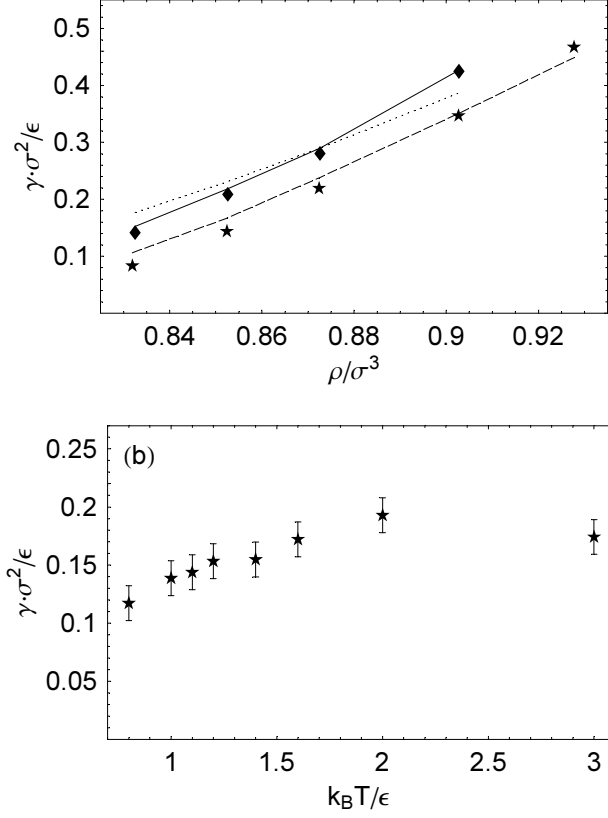


FIG. 8: The surface tension  $\gamma$  for  $\epsilon^* = 5$  ( $\star$ ) and 6 ( $\blacklozenge$ ) as a function of (a) average density at  $T = 1.1$  and (b) temperature at  $\rho = 0.85$ . Error bars represent systematic errors from  $\langle P_{xx} - (P_{yy} + P_{zz})/2 \rangle$  in the bulk regions. The dashed and solid lines in (a) are the surface tension computed using the lattice Boltzmann method for  $\epsilon^* = 5$  and 6, respectively, as discussed in Section V. The dotted line is the surface tension computed using the lattice Boltzmann method with the Flory-Huggins free energy discussed in Appendix B for  $\epsilon^* = 6$ .

from the interfacial profiles of the  $\rho$  and  $\Phi$ . We will discuss this difference below.

The interfacial stress profile is also related to gradients of the density and order parameter. Substituting the expression for the pressure tensor Eq.(12) into Eq.(25) gives,

$$\Gamma(x) = k_B T \left[ K_\rho (\partial_x \rho)^2 + K_\Phi (\partial_x \Phi)^2 + 2K_{\rho\Phi} (\partial_x \rho) (\partial_x \Phi) \right]. \quad (26)$$

The numerical derivatives are computed by first doing a local quadratic fit to the data ( $\rho$  or  $\Phi$ ) over a range of five to seven points (data was collected in bins with width  $0.29\sigma$ ) and then using the derivative of the local fitting function. Figure 10(b) shows the contributions from the various terms in Eq. 26. As is evident from the figure, the only significant contribution to the interfacial stress comes from the  $K_\Phi (\partial_x \Phi)^2$  term. As a result, since the interface

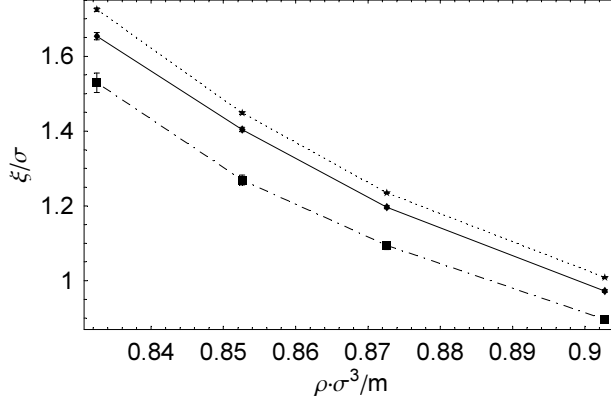


FIG. 9: The interface width for  $\epsilon^* = 6$  as a function of average density calculated from fits of the order parameter  $\Phi$  profile to an error function (◆) and the density profile to a constant minus a Gaussian (★). The width obtained from the stress profile  $\Gamma$  is also shown (■). Lines are only a guide to the eye.

profile for  $\Phi$  is well fit by the error function  $\text{erf}((x - x_0)/\sqrt{2\xi^2})$  we would expect the width obtained from a fit of the stress difference  $\Gamma(x)$  to a Gaussian to give a width  $1/\sqrt{2} \approx 0.71$  of that from the fit to  $\Phi$ . The width we actually measure from  $\Gamma(x)$  is about 0.9 of that obtained from  $\Phi$  (see Fig. 9). That is, the stress profile is wider than expected, a fact that is also obvious from Fig. 10(b). This may be due to a failure of the square gradient theory or may be a result of interface fluctuations not yet taken into account, namely capillary waves.

The widths measured in molecular dynamics simulations are not the intrinsic values but widths broadened by thermal fluctuations. Capillary waves result in the measured time averaged width  $\xi$  being larger than the intrinsic width  $\xi_0$  by [36]

$$\xi^2 = \xi_0^2 + \frac{k_B T}{2\pi\gamma} \ln \left( \frac{L}{\Delta_0} \right), \quad (27)$$

where  $\Delta_0$  is a short scale cutoff.  $\Delta_0$  is expected to be proportional to the intrinsic interface width (fluctuations on length scales shorter than the interface width are not capillary waves). We take  $\Delta_0 \equiv c\xi_0$  where  $\xi_0$  is the intrinsic width of the  $\Phi$  profile and  $c$  is a numerical constant. The bare width from the  $\Phi$  profile is used for  $\xi_0$  since the width from  $\Gamma$  is a derived quantity in the square gradient theory. As all widths in the problem are proportional to the intrinsic width of the  $\Phi$  profile, changing the width used in defining  $\Delta_0$  will change  $c$  but not  $\Delta_0$ .

Following Ref.[36] we verify Eq.(27) by plotting the measured width as a function of system size. This is shown in Fig. 11(a). Fitting the data to the expression  $\xi^2 = a_\delta + b_\delta \ln L$ ,

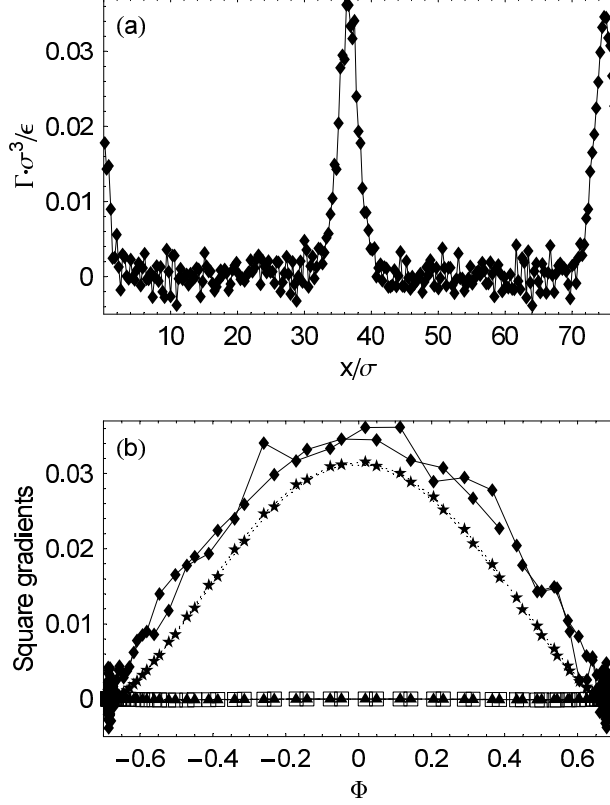


FIG. 10: (a) The interface stress difference  $\Gamma(x) = P_{xx}(x) - (P_{yy}(x) + P_{zz}(x))/2$  for a system with average density  $\rho = 0.83$  and  $\epsilon^* = 6$ . (b) The interface stress difference  $\Gamma$  ( $\diamond$ ) and square gradient contributions  $K_\Phi(\partial_x\Phi)^2$  ( $\star$ ),  $K_\rho(\partial_x\rho)^2$  ( $\square$ ), and  $K_{\rho\Phi}(\partial_x\rho)(\partial_x\Phi)$  ( $\blacktriangle$ ). The elastic constants were taken from the linear response data (the  $\phi^8$  fit was used for  $K_\Phi$ ). Data is for a system with average density 0.83 and  $\epsilon^* = 6$ . Note that due to the periodic boundary conditions there are two interfaces in the system, giving two independent curves in (b).

we find that  $b_\delta = k_B T / (2\pi\gamma)$  to well within measurement errors, as expected from Eq.(27). The other parameter from the fit

$$a_\delta = \xi_0^2 - b_\delta \ln c \xi_0 \quad (28)$$

could be used to obtain  $\xi_0$  if we knew  $c$ . Unfortunately that information is *not* available from this fit alone. In Ref.[36],  $c \equiv 13$  was picked arbitrarily as the smallest number where Eq.(28) had a solution for all the systems considered, including monomers and polymers with up to 30 monomers. There is, however, no reason to believe that  $c$  should be a universal number in this sense.

If we assume that square gradient theory describes the interfaces, just as it works for

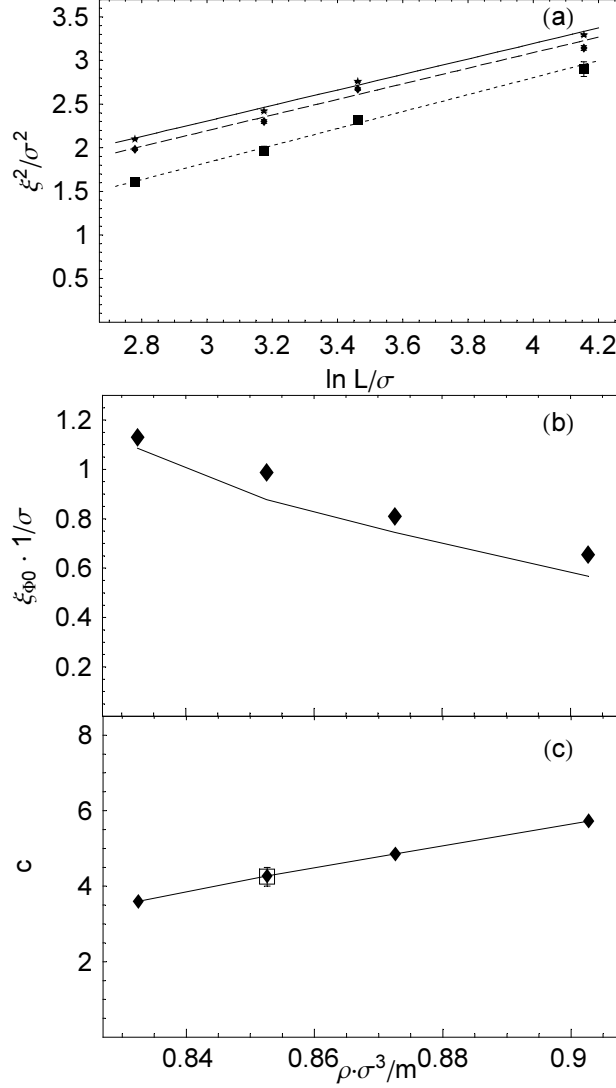


FIG. 11: (a) Dependence of the interfacial widths computed from the  $\Phi$  profile (◆),  $\rho$  profile (★), and  $\Gamma$  (■) as a function of the system size parallel to the interface. The density is 0.85 and  $\epsilon^* = 6$  for all systems. Lines show linear fits to Eq. 27. (b) The intrinsic interface width as a function of average density for the order parameter  $\Phi$  profile from molecular dynamics (◆) and from lattice Boltzmann (line). (c) Parameter  $c$  relating the short scale cutoff  $\Delta_0$  to  $\xi_{\Phi_0}$  calculated using Eq.(29) (◆) and Eq. (28) (□). Data for  $\epsilon^* = 6$  is shown but similar results are obtained for  $\epsilon^* = 5$ .

linear response, then the value of  $c$  can be obtained from the difference in the widths of the  $\Gamma$  and  $\Phi$  profiles. In the square gradient theory the intrinsic widths should obey the relation  $\xi_{\Gamma_0}^2 = \xi_{\Phi_0}^2/2$ , where  $\xi_{\Gamma_0}$  is the intrinsic width of  $\Gamma$  and  $\xi_{\Phi_0}$  the intrinsic width of  $\Phi$ . Based on

Eq.(27), the measured widths,  $\xi_\Phi$  and  $\xi_\Gamma$ , of the  $\Phi$  and  $\Gamma$  profiles should be

$$\begin{aligned}\xi_\Phi^2 &= \xi_{\Phi_0}^2 + \frac{k_B T}{2\pi\gamma} \ln\left(\frac{L}{c\xi_{\Phi_0}}\right), \\ \xi_\Gamma^2 &= \frac{1}{2}\xi_{\Phi_0}^2 + \frac{k_B T}{2\pi\gamma} \ln\left(\frac{L}{c\xi_{\Phi_0}}\right).\end{aligned}\tag{29}$$

Solving these equations simultaneously for  $c$  and  $\xi_{\Phi_0}$  gives the result shown in Fig.11(b). Using Eq.(28), we can also compute  $c$  from the finite size scaling if we use the intrinsic widths obtained from Eq.(29). The agreement seen between these two methods in Fig. 11(c) gives weight to the assumption that square gradient theory describes the interfaces accurately.

We can also assess the consistency of the values of  $K_\Phi$  obtained from the linear response with estimates from interface data. To do this, we assume capillary waves broaden the interface in a Gaussian manner (i.e. the measured shape of the interface is a convolution of the intrinsic shape and a Gaussian distribution of width  $\sqrt{\xi^2 - \xi_0^2}$ ). If we further assume that  $K_\Phi$  is constant and that the intrinsic line shape for  $\Phi$  is reasonably approximated by an error function (which is the case for the broadened shape directly measured), then

$$\left[ \frac{\Gamma(x=0)}{\partial_x \Phi(x=0)} \right]_{MD} = k_B T K_\Phi \frac{\xi_\Phi^2}{\sqrt{2}\xi_\Gamma \xi_{\Phi_0}}.\tag{30}$$

The quantity on the left is the directly measured (capillary broadened) stress difference divided by the gradient of  $\Phi$  at the point where  $\Phi$  crosses zero (center of the interface). The ratio of the length scales,  $\xi_\Phi^2/(\sqrt{2}\xi_\Gamma \xi_{\Phi_0})$ , is about  $1.21 \pm 0.05$  for the interfaces measured. This gives a value of  $K_\Phi$  of  $0.29 \pm 0.03\sigma^5/m^2$ . As  $\Gamma$  (and  $\partial_x \Phi$ ) is peaked at  $\Phi = 0$  and goes to zero as  $\Phi \rightarrow \Phi_{co}$  this measure of  $K_\Phi$  is dominated by the value of  $K_\Phi$  at  $\Phi = 0$ . In the previous section we determined that  $K_\Phi$  is essentially constant near  $\Phi = 0$  and that in this region it should have a value around  $0.286$  to  $0.319\sigma^5/m^2$ . Thus we can be reasonably happy that the elastic constants determined from linear response are consistent with those obtained from the interfaces.

#### IV. FREE ENERGY PARAMETERIZATION

In order to use the information from the molecular dynamics simulations in a mesoscopic model, we also need to parameterize the bulk free energy density  $\psi$ . As we have direct information about  $\psi$  and its various derivatives from the interfacial stress and linear response data, this would not at first appear to be a difficult thing to do. However,  $\psi$  is a function

of both  $\rho$  and  $\Phi$ . The addition of the order parameter means that expressions for obtaining the free energy from the pressure found in standard references [18] are *not* applicable. Fig. 7(c) shows that as one goes through an interface,  $\Phi$  can be reasonably approximated by a quadratic function of the local density  $\rho$ . As a result, distinguishing  $\psi$ 's dependence on  $\Phi$  from that on  $\rho$  using interfacial data alone is extremely difficult. Also, capillary waves change the shape of the interfacial profiles so that getting information about  $\psi$  directly from the interface shape can be misleading. We therefore use the linear response data to do the fits and then compare the resulting surface properties as a test of the parameterization in Section V.

Before deciding on a particular functional form, it is worthwhile to examine what we would like to fit, and to prioritize what is most/least important. Our fit priorities are:

1. Phase diagram/coexistence line ( $\Phi_{co}(\rho)$ ).
2. Linear response of equilibrium phase (compressibility, etc).
3. Surface tension.
4. Interface widths.

The rationale for this choice is fairly simple. Any model incapable of satisfying the first item has little, if any, useful properties. A model capable of reproducing the first two items will at least have a reasonable response to bulk forces. If a model fits the first three items then it should reproduce most macroscopic interfacial behavior. If in addition the fourth item can be fit, then we can reasonably expect it to describe a number of microscopic processes with macroscopic consequences, such as droplet coalescence or pinch-off.

There are a number of free energy functionals commonly used to study fluid mixtures. We found Flory-Huggins theory has too few parameters to satisfy our first two requirements, while a Landau-Ginzburg expansion requires too many, resulting in ambiguous fits. In this section we discuss an alternative parameterization and relegate discussions of Flory-Huggins theory to Appendix B.

To minimize degeneracies in the fitting procedure, we will try to parameterize the free energy in terms of quantities that are directly measured in the molecular dynamics simulations. The partition function we use is a sum of Gaussians centered at  $\pm\Phi_{co}$  plus a third

Gaussian centered at  $\Phi = 0$  whose amplitude is chosen so as to partially cancel the overlap of the other two Gaussians. This results in the free energy density:

$$\begin{aligned} k_B T \psi = & A_0 - \rho k_B T \ln \left[ \exp(-A_2(\Phi - \Phi_{co})^2 / (2\rho k_B T)) \right. \\ & + \exp(-A_2(\Phi + \Phi_{co})^2 / (2\rho k_B T)) \\ & \left. - \exp(-A_2(\Phi^2 + \Phi_{co}^2) / (\rho k_B T)) \right] \end{aligned} \quad (31)$$

where  $A_0$ ,  $A_2$ , and  $\Phi_{co}$  are functions of  $\rho$  to be determined. As we will show, Eq.(31) reproduces the linear response data to within statistical errors essentially by construction. For a single phase system on the coexistence line, but far from the critical point so  $\Phi_{co} \gg 0$ , Eq.(31) simplifies to a more familiar form

$$k_B T \psi = A_0 + \frac{1}{2} A_2 (\Phi - \Phi_{co})^2.$$

The parameters of the free energy functional can be determined directly from our molecular dynamics measurements of the equilibrium state. On the coexistence line ( $\Phi = \pm \Phi_{co}$ ) one can easily show that

$$\frac{\partial^2 \psi}{\partial \rho^2} = \frac{1}{k_B T} \frac{\partial^2 A_0}{\partial \rho^2} + \frac{\partial^2 \psi}{\partial \Phi^2} \left( \frac{d\Phi_{co}}{d\rho} \right)^2, \quad (32)$$

$$\frac{\partial^2 \psi}{\partial \rho \partial \Phi} = - \frac{\partial^2 \psi}{\partial \Phi^2} \left( \frac{d\Phi_{co}}{d\rho} \right), \quad (33)$$

$$\frac{\partial^2 \psi}{\partial \Phi^2} = \frac{A_2}{k_B T} \left( 1 - \exp \left( - \frac{2A_2 \Phi_{co}^2}{\rho k_B T} \right) \right). \quad (34)$$

For states where  $\Phi_{co}$  is significantly greater than zero the last expression reduces to  $\partial^2 \psi / \partial \Phi^2 = A_2$ . The equilibrium hydrostatic pressure is

$$p_0 = \rho \frac{\partial A_0}{\partial \rho} - A_0. \quad (35)$$

By rearranging these equations it is also straightforward to show that along the coexistence line

$$\frac{dp_0}{d\rho} = \rho k_B T \left[ \frac{\partial^2 \psi}{\partial \rho^2} - \frac{\left( \frac{\partial^2 \psi}{\partial \rho \partial \Phi} \right)^2}{\frac{\partial^2 \psi}{\partial \Phi^2}} \right] = \rho \frac{\partial^2 A_0}{\partial \rho^2}, \quad (36)$$

$$\frac{d\Phi_{co}}{d\rho} = - \frac{\frac{\partial^2 \psi}{\partial \rho \partial \Phi}}{\frac{\partial^2 \psi}{\partial \Phi^2}}. \quad (37)$$

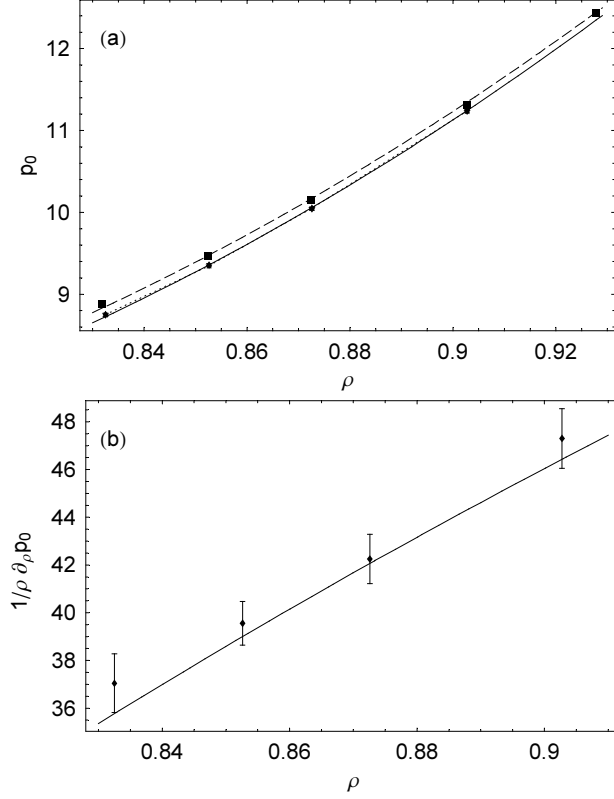


FIG. 12: Fits to (a)  $p_0$  and (b)  $dp_0/d\rho$  which give the parameterization of  $A_0$  in Eq.(38)). In (a), molecular dynamics data is shown for  $\epsilon^* = 5$  (■) and  $\epsilon^* = 6$  (◆) and the solid and dashed lines correspond to the fits described in the main text. The dotted line in (a) (which overlaps with the solid line except at small  $\rho$ ) corresponds to the fits used to determine  $\psi_0$  for the Flory-Huggins model described in Appendix B for  $\epsilon^* = 6$ . In (b) only the  $\epsilon^* = 6$  data is shown.

To use Eq.(31) in the lattice Boltzmann algorithm, we need to choose a functional form for the dependence of the parameters on  $\rho$ . As we have information about both values and derivatives (of  $\Phi_{co}$  for instance), one could use a spline fit to match the measured values exactly. Alternatively, we can pick a functional form for the parameters and fit them over a range of  $\rho$ . For  $A_0$ , a convenient form is

$$A_0 = a_0 + a_1 \rho \ln \rho + a_2 \rho^2. \quad (38)$$

Then from Eq.(35),

$$p_0 = -a_0 + a_1 \rho + a_2 \rho^2 \quad (39)$$

and from Eq.(37)

$$\frac{1}{\rho} \frac{dp_0}{d\rho}|_{co} = \frac{\partial^2 \psi}{\partial \rho^2} - \frac{\left(\frac{\partial^2 \psi}{\partial \rho \partial \Phi}\right)^2}{\left(\frac{\partial^2 \psi}{\partial \Phi^2}\right)} = a_1 \frac{1}{\rho} + 2a_2. \quad (40)$$

A simultaneous fit of  $p_0$  and  $dp_0/d\rho$ , weighted by the statistical errors from the measurements of  $p_0$  and the second derivatives used to obtain  $dp_0/d\rho$ , is shown in Fig.12. The values of the fit parameters are given in Table II.

Similarly, it is straightforward to do a fit of  $\Phi_{co}$  to a quadratic function taking into account the information about  $d\Phi_{co}/d\rho$  (Eq.(37)):

$$\Phi_{co} = b_0 + b_1(\rho - \rho_0) + b_2(\rho - \rho_0)^2, \quad (41)$$

where  $\rho_0 = 0.85 m/\sigma^3$  is a reference density chosen so as to make the statistical errors in the fit parameters given in Table II independent. This fit is shown in Fig. 3. The parameterization of the remaining quantity,  $A_2$ , is done in two steps. First, Eq. (34) is numerically inverted to obtain  $A_2$  at each point using the directly measured  $\Phi_{co}$  and  $\partial^2 \psi / \partial \Phi^2$ . The resulting values are then fit to the function:

$$A_2 = c_0 \exp(c_1(\rho - \rho_0)). \quad (42)$$

The fitted parameters are given in Table II and the resulting fit to  $\partial^2 \psi / \partial \Phi^2$  is shown in Fig. 5(c). An exponential was chosen to fit  $A_2$  rather than a quadratic or other polynomial for two reasons. First, it gave a better fit, and second, the quadratic did not remain monotonic over the full range of interest leading to unphysical effects when extrapolating outside the range of densities where linear response was measured.

One could, in principle, add additional terms to the bulk free energy density that would have *no* impact on the coexistence curve or the linear response data fitted so far. Such a term would be zero and have zero first and second derivatives on the coexistence line. If, in addition, it was peaked at  $\phi = 0$  it would affect the surface tension and interface width. As discussed in the next section, we do not need such terms here but they may be useful in other contexts.

## V. TESTS OF PARAMETERIZATION

To test the above parameterization's description of interface properties we make use of lattice Boltzmann simulations. Lattice Boltzmann simulations were run for the same system

$\epsilon^*$	5	6
$a_0$	$-43.92 \pm 5.72 \frac{m}{\sigma\tau^2}$	$-43.78 \pm 5.8 \frac{m}{\sigma\tau^2}$
$a_1$	$-113.8 \pm 13.0 \frac{\sigma^2}{\tau^2}$	$-114.0 \pm 13.4 \frac{\sigma^2}{\tau^2}$
$a_2$	$86.04 \pm 7.42 \frac{\sigma^5}{m\tau^2}$	$86.37 \pm 7.7 \frac{\sigma^5}{m\tau^2}$
$b_0$	$0.695 \pm 0.004 \frac{m}{\sigma^3}$	$0.739 \pm 0.003 \frac{m}{\sigma^3}$
$b_1$	$3.37 \pm 0.15$	$2.69 \pm 0.12$
$b_2$	$-12.0 \pm 1.6 \frac{\sigma^3}{m}$	$-9.5 \pm 1.6 \frac{\sigma^3}{m}$
$c_0$	$2.011 \pm 0.060 \frac{\sigma^5}{m\tau^2}$	$2.827 \pm 0.007 \frac{\sigma^5}{m\tau^2}$
$c_1$	$20.40 \pm 0.67 \frac{\sigma^3}{m}$	$21.70 \pm 0.09 \frac{\sigma^3}{m}$

TABLE II: Table of parameters for the free energy  $\psi$  in Eq. (31). Parameters are defined in Eqs. (38), (41), and (42). As for the elastic constants given in Table I, the data were measured for  $0.82 m/\sigma^3 < \rho < 0.925 m/\sigma^3$  and care should be taken in extrapolating outside of the measured range.

size and compositions as the molecular dynamics simulations. We first verified that the lattice Boltzmann program correctly reproduced the bulk data. Surface tensions were then computed from the integral of the stress difference through the interface, Eq.(25), just as we did for the molecular dynamics simulations. Figure 8 shows the surface tension computed from the lattice Boltzmann program using the elastic constants and  $\psi$  parameters from Table II. Although the parameterization only used the linear response data, the surface tensions are very close to the molecular dynamics results, although they tend to be slightly higher. As discussed in Section III B, the interfacial properties are dominated by the peak in the free energy and value of the elastic constants near  $\phi = 0$ . All the fits to the data were for values of  $\phi > 0.73$ , and it is remarkable that such an extrapolation works so well.

Due to capillary waves we cannot directly compare the full interfacial profiles of the density and order parameter to the molecular dynamics. However, we can verify that the total mass deficit at the interface is correct. This can be calculated from the integral under the dip in plots like Fig. 7(b) or from the increase in the density far from the interface that compensates for the dip. For example, consider a molecular dynamics simulation where the total average system density is  $\rho = 0.85m/\sigma^3$ ,  $k_B T/\epsilon = 1.1$ , and with length  $L_x = 74.36\sigma$ . We find that the density far from the interface  $\rho = 0.8526 \pm 0.0001m/\sigma^3$  is larger than the

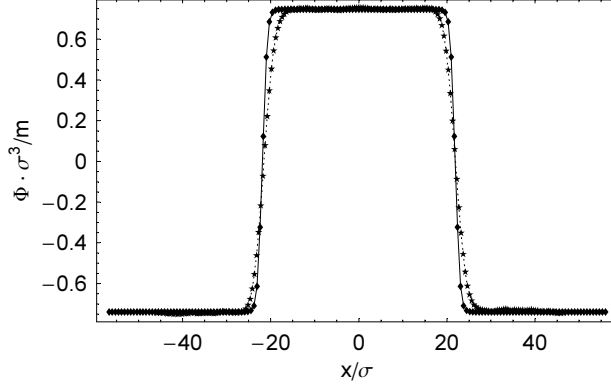


FIG. 13: Order parameter profile on a cut going through the center of the drop. Note that the molecular dynamics profile has been smeared somewhat due to capillary waves and Brownian motion of the drop that are not present in the lattice Boltzmann simulation.

system average to make up for the deficit at the interface. A lattice Boltzmann simulation with the same system size and total average density shows exactly the same mass increase in the bulk.

Figure 11(a) shows that there is also reasonable agreement between the intrinsic widths computed via the lattice Boltzmann and the molecular dynamics. Although in this case the intrinsic widths measured from the lattice Boltzmann tend to be a bit smaller.

To test our model parameterization in a different geometry we examined a cylindrical drop. In three dimensions, a cylinder of fluid is unstable to spherical droplet formation. We avoided this instability by making the radius  $R$  of the droplet bigger than the system size along the axis of the cylinder ( $y$ -axis). Specifically,  $R = 24.5\sigma$ ,  $L_y = 16\sigma$ , and  $L_x$  and  $L_z$  were about  $100\sigma$ . For a density of  $\rho = 0.85m/\sigma^3$  this required 147456 molecules and  $10^7$  time steps were needed to get good statistics, which is reasonably large for a molecular dynamics simulation. The only significant difference between the molecular dynamics simulation and the lattice Boltzmann method is the presence of thermal noise. In the molecular dynamics simulation this causes the drop to undergo Brownian motion. In order to do a meaningful comparison we limited this effect by periodically shifting the system so that the center of mass of the drop remained at  $x = z = 0$ .

Figure 13 compares profiles of the order parameter through the center of the drop from molecular dynamics and lattice Boltzmann simulations. The molecular dynamics profile is broadened slightly by capillary waves and Brownian motion. Neither effect is present in the

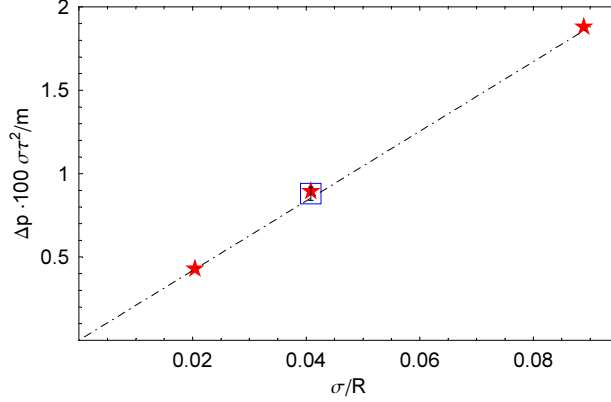


FIG. 14: Laplace pressure between the inside and outside of a cylindrical fluid “drop”, versus the curvature  $1/R$ , where  $R$  is the drop radius. Results from lattice Boltzmann simulations (★) and molecular dynamics simulations (□) are consistent with each other and with the straight line prediction from continuum theory Eq.43.

lattice Boltzmann simulation. The two methods both show that  $\Phi$  is lower by  $0.01m/\sigma^3$  than the equilibrium bulk value in the center of the drop. The reason for the drop in  $\Phi$  is that the interfacial curvature produces a pressure difference  $\Delta p_0$  between the inside and outside called the Laplace pressure. This also increases the density in the drop. For  $R = 24.5\sigma$  the density difference from lattice Boltzmann simulations is  $0.00867m/\sigma^3$ , which agrees with the value of  $0.009 \pm 0.002m/\sigma^3$  from molecular dynamics. For a macroscopic cylinder, the pressure difference between the inside and outside of the drop should scale with the radius as [37]

$$\Delta p_0 = \gamma/R, \quad (43)$$

where  $\gamma$  is the surface tension measured in the molecular dynamics simulation of a flat interface. As can be seen in Figure 14, both the molecular dynamics simulation and the lattice Boltzmann results follow this relationship very well.

## VI. MODEL COMPARISONS

It is worthwhile to compare our findings to commonly used assumptions in mesoscale modeling of binary fluids. We first consider the assumption of incompressibility that is often used for both simple and binary fluids. For bulk fluids, including those examined here, this is a very reasonable assumption as  $\partial^2\psi/\partial\rho^2$  is very large compared to other second derivatives

of the free energy (cf. Section III A). However, due to the fact that  $K_\rho$  is negative, the fluid can be very soft on the short length scales characteristic of interface widths. This invalidates the assumption of incompressibility in the interfacial region.

As noted in Section II B, the density drops in the interfacial region to reduce unfavorable 1 – 2 molecular interactions and hence the free energy. The quantitative impact of density changes can be seen by considering the change in the free energy barrier (Eq. 31) in the interfacial region. Due to the change in density in the interface, we find that  $A_2$  drops down to around 50 percent of its value in the bulk. This reduction in  $A_2$  spreads the Gaussian functions in Eq.(31) thereby reducing the barrier between the  $\pm\Phi_{co}$  states. There is a corresponding reduction in the total interfacial tension which is given by the integral of  $\Gamma(x)$  through the interface (Eqs. 24 and 25). Using the Euler-Lagrange equations (Eqs. 7 and 8) one can show that  $\Gamma(x)$  is directly related to the free energy barrier:  $\Gamma(x) = k_B T \psi - A_0$ . To see the impact of density changes in the interface we can compare the integral of  $\Gamma(x)$  using the  $\Phi$  profile from the lattice Boltzmann simulation combined with either a  $\rho$ -dependent value of  $A_2$  or a constant bulk value of  $A_2$ . We find that including density variations reduces the surface tension by a factor of 2 – 4 relative to incompressible models. Thus the density drop at the interface is not a negligible effect for any quantitative study involving interfaces.

As mentioned before, the Flory-Huggins theory has too few parameters to obtain a precise fit to both the coexistence curve and the linear response. As discussed in Appendix B, we can obtain the Flory-Huggins  $\chi$  parameter from a fit to the coexistence curve shown in Fig. 3. The resulting linear response seen in Fig. 5, while not in quantitative agreement with MD results, should be adequate for qualitative work. The Flory-Huggins prediction for the surface tensions seen in Fig. 8 is actually remarkably good. It is important to note however, that we have allowed  $\chi$  to vary with the local density. As a result,  $\chi$  drops significantly in the interfacial region due to the interfacial density drop. This reduces the surface tension by a large factor compared to incompressible models, just as the reduction in  $A_2$  discussed above did. As most implementations of Flory-Huggins models for simulations assume incompressibility, such models will have surface tensions that are a factor of 2 – 4 too large.

It is commonly found in lattice Boltzmann simulations that a stationary droplet in quiescent conditions will develop a flow field around it similar to that shown in Fig. 15(a) [26, 38]. It has recently been pointed out that these spurious velocities arise due to discretization er-

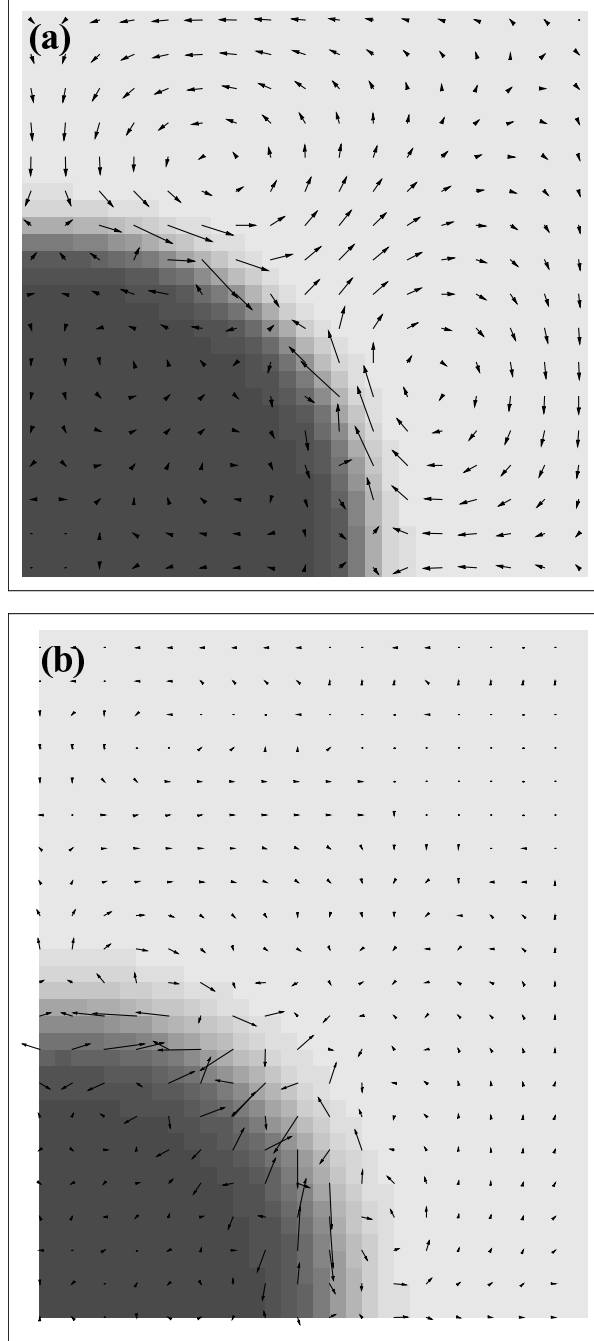


FIG. 15:  $\Phi$  field (shading) and velocity field (vectors) for one quadrant of a stationary cylindrical fluid “drop”. In (a), a standard model from the literature [26] was used and in (b), the model we have matched to the molecular dynamics data. In units where  $dx = dt = 1.0$ , the largest velocity vector is  $1.2 \times 10^{-4}$  in (a) and  $1.5 \times 10^{-6}$  in (b). Note that the velocities in (b) would not be visible if we had used the same scale as that used in (a). The radius of the drop in (b) is slightly smaller but this should only increase spurious velocities compared to (a).

rors [38] which drive the spurious currents. For our model, fitted to the molecular dynamics data, we can estimate the truncation error from the discretization to be  $\sim 10^{-6}$  and the velocities seen at the interface in Fig. 15(b) are indeed of this magnitude (in lattice units). The discretization error for the standard model from the literature used to produce Fig. 15(a) should also be  $\sim 10^{-6}$  however the spurious velocities observed are nearly 100 times greater. Further, the flow field for the standard model includes considerable vorticity and significant flows far from the interface itself. This suggests that discretization errors are driving an unstable (and possibly unphysical) mode of the standard system leading to much larger spurious velocities. In our model, this mode is absent and discretization errors are not exaggerated.

One possible origin for unphysical modes in Fig. 15(a) and similar models is related to the time scales used. In situations where the model parameters have not been measured so that the length and time scales are uncertain, the viscosity and diffusion constant may be set for convenience. Normally this would not affect equilibrium properties, but if unphysical choices are made, unstable modes like the ones being driven by the spurious velocities may be set up. For instance, unstable modes may appear if the diffusion constant is set so large that material can diffuse faster than it can flow. To ensure that this is not the case in our model, we have used a viscosity and diffusion constant that were measured in molecular dynamics simulations for similar fluids,  $\eta \approx 3 \epsilon \tau / \sigma$  [39] and  $D = 0.1 \sigma^2 / \tau$  [15].

## VII. SUMMARY AND CONCLUSIONS

This paper presents detailed molecular dynamics simulation results for a binary mixture of simple fluids and uses them to construct a square gradient theory that can be used for realistic mesoscale modeling. The MD simulations examine the linear response, interfacial tension, and interfacial width as a function of density, temperature, and the repulsion between different species. Two remarkable conclusions arise from the linear response results (Sec. III A). The first is that a square gradient theory is capable of quantitatively describing the response down to wavelengths that are comparable to the molecular spacing ( $< 2\sigma$ ). This implies that mesoscale models may have a much wider range of applicability than might be expected. The second surprising result is that the elastic constant for density changes,  $K_\rho$ , is *negative*. As a result, the system is more susceptible to fluctuations at shorter wavelengths.

Indeed, it is only stabilized at small scales by atomic discreteness [31]. This prevents density fluctuations on length scales less than  $\sigma$  where the total response coefficient  $L_{\rho\rho}$  becomes negative.

Studies of interfacial properties (Sec. IIIB) show that the common assumption of incompressibility is not valid. This is related to the observation that  $K_\rho < 0$ , which lowers the free energy cost of localized density fluctuations. Although the density change is small, it can reduce the interfacial tension by a factor of 2–4.

The density, order parameter and surface stress were evaluated as a function of position normal to the interface, and used to determine interfacial widths. The variation in width with system size is consistent with broadening by thermal capillary waves. Comparing the scaling of widths from the stress and order parameter, allows all the parameters of the capillary model to be determined independently.

Fits to linear response about states on the coexistence curve showed an impressive ability to predict interfacial properties. Predicted values of the surface tension (Fig. 8) and the density deficit at the interface (Sec. V) are nearly within the statistical error bars of the MD results. This is particularly surprising given the large change in order parameter through the interface and small interface width (Fig. 9). The main discrepancy between the MD results and mesoscale simulations is that the latter do not include interface broadening by capillary waves.

Many LB models have been found to produce spurious velocities around curved interfaces. While some discretization error is expected, it appears that these errors are amplified when the time scales in the LB model are chosen arbitrarily or for computational convenience. Using time scales derived from MD simulations prevents unphysical choices that, for example, allow material to diffuse more rapidly than it flows. Fig. 15 shows that using MD parameters can reduce spurious velocities by around three orders of magnitude.

The final square gradient theory (Table II) has a simple analytic form and provides an excellent fit to all MD results for phase coexistence, linear response, and interfacial properties over a wide range of densities. This is particularly important for future studies of nonequilibrium phenomena such as pinchoff or contact line motion. Dynamic processes will lead to variations in local density and order parameter that will in turn lead to variations in local interfacial stress. These variations will have important implications for the dynamics, producing Marangoni-like effects or changing the wavelength dependent response of the

interface. Our results for the influence of density changes on interfacial tension indicate that these effects may be quite large. While simpler theories (e.g. Appendix B) may be able to describe equilibrium configurations, they do not include these important dependences on local density. More complex theories that are not guided by MD results are unlikely to include important effects such as a negative  $K_\rho$ . It will be interesting to explore the dynamic consequences of such effects in future work.

## Acknowledgments

This material is based upon work supported by the National Science Foundation under Grant No. 0083286. The molecular dynamics simulations were performed using a variant of LAMMPS from Sandia National Laboratories [19].

## APPENDIX A: ELASTIC CONSTANT VARIATIONS

Frequently the free energy is parameterized as a function of the individual species densities  $\rho_1$  and  $\rho_2$ . The free energy can then be expressed as

$$\mathcal{F} = k_B T \int d\mathbf{r} \left\{ \psi + \frac{1}{2} K_{11} (\nabla \rho_1)^2 + \frac{1}{2} K_{22} (\nabla \rho_2)^2 + K_{12} \nabla \rho_1 \cdot \nabla \rho_2 \right\}. \quad (\text{A1})$$

The resulting elastic constants are linearly related to those in Eq.(3):  $K_{11} = K_\rho + K_\Phi + 2K_{\rho\Phi}$ ,  $K_{11} = K_\rho + K_\Phi - 2K_{\rho\Phi}$ , and  $K_{12} = K_\rho - K_\Phi$ .

Another order parameter that is often used, the relative concentration, is  $\phi = \Phi/\rho$ . The free energy becomes

$$\mathcal{F} = k_B T \int d\mathbf{r} \left\{ \psi + \frac{1}{2} k_\rho (\nabla \rho)^2 + \frac{1}{2} k_\phi (\nabla \phi)^2 + k_{\rho\phi} \nabla \rho \cdot \nabla \phi \right\}. \quad (\text{A2})$$

These elastic constants have a more complex mapping to those in the main text,

$$K_\rho = k_\rho + k_\phi \Phi^2 / \rho^4 - 2k_{\rho\phi} \Phi / \rho^2, \quad (\text{A3})$$

$$K_\Phi = k_\phi / \rho^2, \quad (\text{A4})$$

$$K_{\rho\Phi} = k_{\rho\phi} / \rho - k_\phi \Phi / \rho^3. \quad (\text{A5})$$

It is obvious from these relations that the  $K$ 's and  $k$ 's can not both be independent of  $\rho$  or  $\Phi$ . There can be advantages to using either  $\phi$  or  $\Phi$  in different physical situations. It turns out that for linear response measurements and for the lattice Boltzmann algorithm it is convenient to work with  $\Phi$ .

As the elastic constants can vary as a function of  $\Phi$  and  $\rho$  this should, in principle, be taken into account in Eq.(8). For the elastic constants used in the main text, the full Euler-Lagrange equations are

$$\begin{aligned} \mu_\rho = & \frac{\partial\psi}{\partial\rho} - K_\rho\nabla^2\rho - K_{\rho\Phi}\nabla^2\Phi - \frac{1}{2}\frac{\partial K_\rho}{\partial\rho}(\nabla\rho)^2 + \\ & \left[\frac{1}{2}\frac{\partial K_\Phi}{\partial\rho} - \frac{\partial K_{\rho\Phi}}{\partial\Phi}\right](\nabla\Phi)^2 - \frac{\partial K_\rho}{\partial\Phi}\nabla\rho \cdot \nabla\Phi, \end{aligned} \quad (\text{A6})$$

$$\begin{aligned} \mu_\Phi = & \frac{\partial\psi}{\partial\Phi} - K_\Phi\nabla^2\Phi - K_{\rho\Phi}\nabla^2\rho - \frac{1}{2}\frac{\partial K_\Phi}{\partial\Phi}(\nabla\Phi)^2 + \\ & \left[\frac{1}{2}\frac{\partial K_\rho}{\partial\Phi} - \frac{\partial K_{\rho\Phi}}{\partial\rho}\right](\nabla\rho)^2 - \frac{\partial K_\Phi}{\partial\rho}\nabla\Phi \cdot \nabla\rho. \end{aligned} \quad (\text{A7})$$

Clearly it would be desirable if some of these terms, especially those involving variations of the elastic constants, were negligible. For the linear response regime it is straightforward to show that these additional terms are order  $\delta^2$  (cf. Equation (23)). However, we must still investigate their importance for interfaces.

Figure 16 shows various contributions from gradients to the potentials of Eq. (A6) and (A7) in a typical interface. As can be seen, the terms that dominate have been kept in Eqs. (7) and (8). The remaining terms are quite small, or essentially zero, thus justifying ignoring them in the main text. Note that some terms that are quite small in interfaces, such as  $K_{\rho\Phi}\nabla^2\rho$  in  $\mu_\Phi$ , are required when looking at the linear response where  $\nabla\rho$  and  $\nabla\Phi$  are of comparable magnitude.

## APPENDIX B: FITS TO FLORY-HUGGINS FREE ENERGY

There are a number of free energy functionals in common use to study fluid mixtures. For polymer mixtures, the Flory-Huggins free energy density is most commonly used. For monomers the free energy density divided by  $k_B T$  is [13]

$$\psi_{FH} = \rho_1 \ln\left(\frac{\rho_1}{\rho}\right) + \rho_2 \ln\left(\frac{\rho_2}{\rho}\right) + \chi \frac{\rho_1 \rho_2}{\rho} \quad (\text{B1})$$

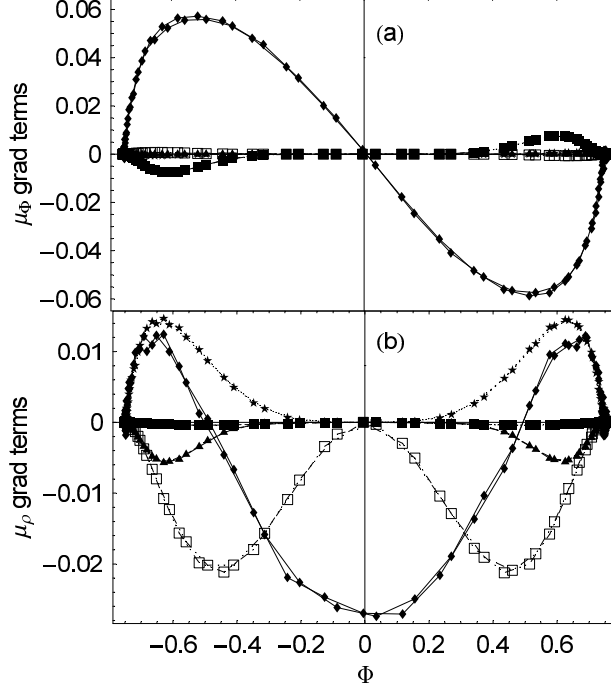


FIG. 16: The individual gradient term contributions to the potentials (a)  $\mu_\Phi$  (Eq.(A7)) and (b)  $\mu_\rho$  (Eq.(A6)) through two interfaces in a system at average density  $\rho = 0.85$  with  $\epsilon^* = 6$ . For  $\mu_\Phi$ , the term  $K_\Phi \nabla^2 \Phi$  ( $\blacklozenge$ ) dominates,  $\frac{1}{2}(\partial K_\Phi / \partial \Phi)(\nabla \Phi)^2$  ( $\blacksquare$ ) is small but visibly different from zero, and  $\frac{1}{2}(\partial K_\rho / \partial \Phi)(\nabla \rho)^2$  ( $\star$ ),  $(\partial K_{\rho\Phi} / \partial \rho)(\nabla \rho)^2$  ( $\square$ ), and  $(\partial K_\Phi / \partial \rho) \nabla \Phi \cdot \nabla \rho$  ( $\blacktriangle$ ) are effectively zero. (b) For  $\mu_\rho$  the significant terms are  $K_\rho \nabla^2 \rho$  ( $\blacklozenge$ ),  $K_{\rho\Phi} \nabla^2 \Phi$  ( $\star$ ) and  $(\partial K_{\rho\Phi} / \partial \Phi)(\nabla \Phi)^2$  ( $\square$ ). The  $\frac{1}{2}(\partial K_\Phi / \partial \rho)(\nabla \Phi)^2$  ( $\blacktriangle$ ) term is small but visibly different from zero. The other terms,  $\frac{1}{2}(\partial K_\rho / \partial \rho)(\nabla \rho)^2$  ( $\blacksquare$ ) and  $(\partial K_\rho / \partial \Phi) \nabla \rho \cdot \nabla \Phi$  ( $\triangle$ ) are effectively zero.

where  $\chi$  is the only free parameter. This is just a modified entropy of mixing and, in order to obtain the bulk pressure, one must add to this an additional function  $\psi_0$  of  $\rho$  alone,

$$\psi = \psi_0 + \psi_{FH}. \quad (\text{B2})$$

If one were to follow the spirit of the derivation of the Flory-Huggins model,  $\psi_0$  should be determined primarily from the entropy of an ideal gas plus some quadratic terms to correct for energy interactions. In practice it is unrealistic to expect such a construction to work. We shall use the same form for  $\psi_0$  as we used for  $A_0$  in Eq.(38). There is also some ambiguity in the definition of the  $\chi$  term in the Flory-Huggins free energy. Some authors use a slightly different term,  $\chi \rho_1 \rho_2 / (v \rho^2)$  where  $v$  is a reference volume [40]. If we allow  $\chi$  to be a function of  $\rho$  then both terms are equivalent but the meaning of  $\chi$  will be slightly different.

We obtain  $\chi$  by fitting  $\Phi_{co}$  and  $d\Phi_{co}/d\rho$  as a function of  $\rho$ . In the bulk states  $\mu_\Phi$  is zero and there are no gradients so that Eq.(8) requires that on the coexistence line

$$0 = \frac{\partial\psi}{\partial\Phi} = \frac{\partial\psi_{FH}}{\partial\Phi} = \frac{1}{2} \ln \left[ \frac{1 + \Phi/\rho}{1 - \Phi/\rho} \right] - \frac{1}{2} \chi \frac{\Phi}{\rho}. \quad (\text{B3})$$

Eq.(37) also holds, and if one evaluates these derivatives for the Flory-Huggins free energy one can obtain the relation

$$\left( \frac{1}{1 + \Phi/\rho} + \frac{1}{1 - \Phi/\rho} \right) \left( \frac{\Phi}{\rho} + \frac{d\Phi_{co}}{d\rho} \right) = \chi \left( \frac{\Phi}{\rho} + \frac{d\Phi_{co}}{d\rho} \right) - \Phi \frac{\partial\chi}{\partial\rho}, \quad (\text{B4})$$

where  $d\Phi_{co}/d\rho$  is evaluated using Eq.(37) and the measured values of the second derivatives. If we take  $\chi$  to be a quadratic function of density,

$$\chi = \chi_0 + \chi_1\rho + \chi_2\rho^2, \quad (\text{B5})$$

then we can do a simultaneous fit to these two equations using a straightforward weighted linear regression (there should not be any conflict between them as we are just fitting  $\Phi_{co}(\rho)$  and the derivative of this function  $d\Phi_{co}/d\rho$ ). The weights are computed from the statistical errors of the measurements of  $\Phi_{co}$  and the second derivatives. We use standard methods to find the statistical errors of the derived quantities. The resulting fits are shown in Fig. 17 and the parameters are given in Table III.

Next we fit the bulk pressure  $p_0$  to obtain  $\psi_0$ . Unlike the fits of the equilibrium  $p_0$  in the main text, which involved only  $A_0$ , there is now a contribution from the  $\Phi$  dependent terms in the free energy. In particular,

$$p_0 = \rho \frac{\partial\psi_0}{\partial\rho} - \psi_0 + \frac{1}{4} k_B T (\rho^2 - \Phi^2) \frac{\partial\chi}{\partial\rho}. \quad (\text{B6})$$

One could, in principle, also use the information about  $dp_0/d\rho$  that we used in fitting  $A_0$  for the single phase free energy. However, the additional terms make a combined fit extremely messy and of dubious value. One still needs a parameterization of  $\psi_0$  in terms of  $\rho$  and we use the same functional form as was used for  $A_0$  (although the numerical values for  $a_{00}$  etc. will, or course be different). The resulting fit to  $p_0$  is shown as a dashed line in Fig. 12 and the parameters are given in Table III.

As all parameters in the Flory-Huggins free energy are now determined, we can now compare the quantities not explicitly used in the fits. Fig. 5 shows the second derivatives of the

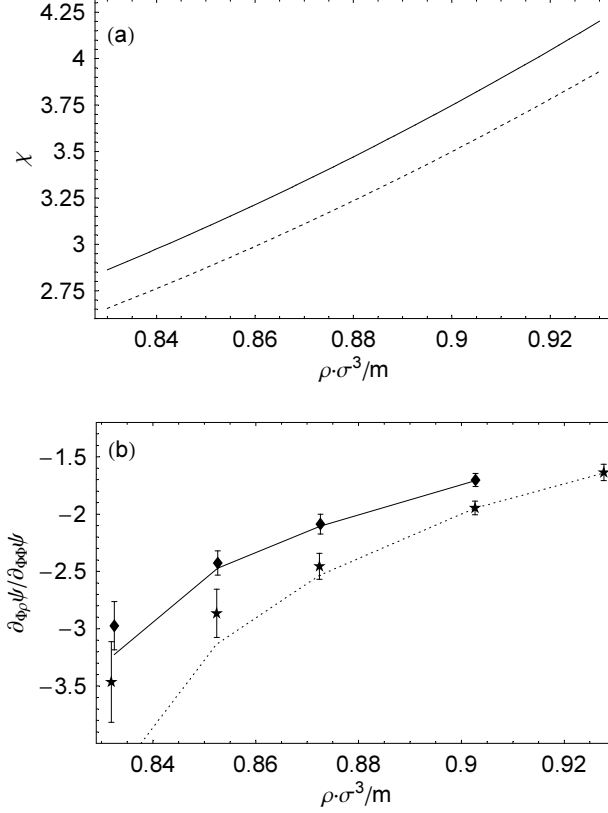


FIG. 17:  $\chi$  parameter (a) obtained from the fits to  $\Phi_{co}(\rho)$  (Fig. 3) and  $d\Phi_{co}/d\rho$  (b). Solid and dotted lines correspond to fits for  $\epsilon^* = 6$  and 5 respectively. Molecular dynamics data in (b) are for  $\epsilon^* = 5$  ( $\star$ ) and 6 ( $\blacklozenge$ ).

bulk free energy as measured from linear response in the molecular dynamics simulations and from the fits. The Flory-Huggins theory overestimates the concavity of the free energy minima. Fig. 8 shows the surface tension derived from a lattice Boltzmann implementation of the fit to the Flory-Huggins theory. The agreement is remarkably good. However, Flory-Huggins normally assumes incompressibility. If we had assumed that the density, and therefore  $\chi$  was constant, the surface tension would be much too large.

It is also worthwhile to compare the values of  $\chi$  obtained here to other methods of estimating  $\chi$ . For long polymers at  $\rho = 0.85m/\sigma^3$ , Grest and coworkers [13] have estimated  $\chi$  in two ways. Using a so-called one-fluid approximation, they estimate  $\chi \approx 0.76\epsilon^*\epsilon/k_B T$ . Using an incompressible random phase approximation to evaluate the static structure factor, they obtain a larger value of  $\chi \approx 1.0\epsilon^*\epsilon/k_B T$ . Our results correspond to a somewhat smaller value of about  $0.54\epsilon^*\epsilon/k_B T$ , which is not surprising given that we consider simple monomers.

$\epsilon^*$	5	6
$a_0$	$-31.51 \pm 2.9 \frac{m}{\sigma\tau^2}$	$-26.50 \pm 6.3 \frac{m}{\sigma\tau^2}$
$a_1$	$-92.33 \pm 6.7 \frac{\sigma^2}{\tau^2}$	$-80.18 \pm 14 \frac{\sigma^2}{\tau^2}$
$a_2$	$77.0 \pm 3.8 \frac{\sigma^5}{m\tau^2}$	$69.7 \pm 8.3 \frac{\sigma^5}{m\tau^2}$
$\chi_0$	$10.15 \pm 4.7$	$10.68 \pm 5.0$
$\chi_1$	$-28.47 \pm 10.4 \frac{\sigma^3}{m}$	$-29.78 \pm 11.21 \frac{\sigma^3}{m}$
$\chi_2$	$23.42 \pm 5.7 \frac{\sigma^6}{m^2}$	$24.52 \pm 6.32 \frac{\sigma^6}{m^2}$

TABLE III: Table of parameters for the Flory-Huggins free energy given in Eq.s (B1) and (B2). Parameters are defined in Eqs. (38) and (B5). As for the parameters given in the main text, the data were measured for  $0.82m/\sigma^3 < \rho < 0.925m/\sigma^3$  and care should be taken in extrapolating outside of the measured range.

- 
- [1] D.M. Anderson, G.B. McFadden and A.A. Wheeler, Annu. Rev. Fluid Mech. **30**, 139 (1998).
  - [2] S. Chen and G.D. Doolen, Annu. Rev. Fluid Mech. **30**, 329 (1998).
  - [3] C. Denniston, E. Orlandini, J.M. Yeomans, Comp. and Theor. Poly. Sci. **11**, 389 (2001).
  - [4] P.D. Olmsted, O. Radulescu, and C.-Y. David Lu, J. Rheology **44** 256 (2000); C.-Y David Lu, P.D. Olmsted, and R.C. Ball, Phys. Rev. Lett. **84**, 642 (2000).
  - [5] J.M. Yeomans, Ann. Rev. Comp. Phys. VII, ed. D. Stauffer, 61 (1999).
  - [6] M.P. Brenner, X.D. Shi, and S.R. Nagel, Phys. Rev. Lett. **73**, 3391 (1994).
  - [7] L. Oddershede and S.R. Nagel, Phys. Rev. Lett. **85** 1234 (2000).
  - [8] I.Cohen, H.Li, J.L. Hougland, M. Mrksich, and S.R. Nagel, Science **292**, 265 (2001).
  - [9] P.A. Thompson and M.O. Robbins, Phys. Rev. Lett. **63**, 766 (1989); P.A. Thompson, W.B. Brindkerhoff, and M.O. Robbins, J. Adhesion Sci. Techno. **7**, 535 (1993).
  - [10] H.-Y. Chen, D. Jasnow, and J. Vinals, Phys. Rev. Lett. **85**, 1686 (2000).
  - [11] V. Ganesan and H. Brenner, Phys. Rev. Lett. **82**, 1333 (1999); H. Brenner and V. Ganesan, Phys. Rev. E **61**, 6879 (2000).
  - [12] H.-P. Deutsch and K. Binder, Macromolecules **25**, 6214 (1992); and references therein.
  - [13] G.S.Grest, M.-D. Lacasse, K. Kremer, and A.M. Gupta, J. Chem. Phys. **105**, 10583 (1996).

- [14] S. Barsky and M.O. Robbins, Phys. Rev. E **63**, 021801 (2001); *ibid.* **65**, 021808 (2002).
- [15] C. Denniston and M.O. Robbins, Phys. Rev. Lett. **87**, 178302 (2001).
- [16] C. Denniston and M.O. Robbins, *Computer Simulation Studies in Condensed Matter Physics XV*, Eds. D.P. Landau, S.P. Lewis, and H.B. Schuttler (Springer Verlag, Heidelberg, Berlin, 2002).
- [17] G.S. Grest, K. Kremer, Phys Rev A **33**, 3628 (1986).
- [18] M.P. Allen and D.J. Tildesley, *Computer Simulation of Liquids*, (Clarendon Press, Oxford, 1987).
- [19] S. J. Plimpton, R. Pollock, M. Stevens, "Particle-Mesh Ewald and rRESPA for Parallel Molecular Dynamics Simulations", in Proc. of the Eighth SIAM Conference on Parallel Processing for Scientific Computing, Minneapolis, MN, March 1997; S. J. Plimpton, "Fast Parallel Algorithms for Short-Range Molecular Dynamics", J. Comp. Phys., **117**, 1-19 (1995).
- [20] J.H. Irving and J.G. Kirkwood, J. Chem. Phys. **18**, 817 (1950).
- [21] L. Mistura, J. Chem. Phys. **83**, 3633 (1985); Inter. J. Thermophys. **8**, 397 (1987); J.S. Rowlinson, Proc. R. Soc. London Ser. A **402**, 67 (1985); J. Chem. Thermodyn. **25**, 449 (1993).
- [22] E. Wajnrib, A.R. Altenberger, and J.S. Dahler, J. Chem. Phys. **103**, 9782 (1995).
- [23] V. Talanquer and D. W. Oxtoby, J. Chem. Phys. **104**, 1993 (1996).
- [24] S. Iatsevitch and F. Forstmann, J. Chem. Phys. **107**, 6925 (1997).
- [25] I. Napari, A. Laaksonen, V. Talanquer, D.W. Oxtoby, J. Chem. Phys. **110**, 5906 (1999).
- [26] M.R. Swift, E. Orlandini, W.R. Osborn, and J.M. Yeomans, Phys. Rev. E **54**, 5041 (1996).
- [27] H. Goldstein, *Classical Mechanics, 2nd Edition*, (Addison-Wesley Pub. Co., Reading MA, 1980).
- [28] D.J. Holdych, D. Rovas, J.G. Georgiadis, and R.O. Buckius, Int. J. of Mod. Phys. C **9**, 1393 (1998).
- [29] M. Criado-Sancho, J. Casas-Vazquez, and D. Jou, Phys. Rev. E **56**, 1887 (1997).
- [30] C. Denniston, E. Orlandini, and J.M. Yeomans, Phys. Rev. E **63**, 056702 (2001).
- [31] Stability could be enforced by adding a higher order gradient with a positive coefficient. However, a very high order may be needed and this would complicate any numerical scheme without providing a clear benefit.
- [32] S. Toxvaerd and J. Stecki, J. Chem. Phys. **102**, 7163 (1995); *ibid* **103**, 4352 (1995).
- [33] E. Diaz-Herrera, J. Alejandre, G. Ramirez-Santiago, and F. Forstmann, J. Chem. Phys. **110**,

- 8084 (1999).
- [34] G. Grest, M.-D. Lacasse, and M. Murat, in *Computer Simulation Studies in Condensed Matter Physics X*, pg. 23, Eds. D.P. Landau, S.P. Lewis, and H.B. Schuttler (Springer Verlag, Heidelberg, Berlin, 1998).
  - [35] J.G. Kirkwood and F.P. Buff, J. Chem. Phys. **17**, 338, (1949).
  - [36] Martin-D. Lacasse, G.S. Grest, and A.J. Levine, Phys. Rev. Lett. **80**, 309 (1998).
  - [37] L.D. Landau and E.M. Lifshitz, *Fluid Mechanics*, (Pergamon Press, Oxford, 1987).
  - [38] A.J. Wagner, Int. J. Mod. Physics **17**, 193 (2003).
  - [39] P.A. Thompson and M.O. Robbins, Phys. Rev. A **41**, 6830 (1990).
  - [40] R.G. Larson, *The Structure and Rheology of Complex Fluids*, (Oxford University Press, Oxford, 1999).